EXPERIMENTAL INVESTIGATION OF THERMAL ENERGY STORAGE (TES) PLATFORM USING PHASE CHANGE MATERIALS (PCM) INTEGRATED WITH HEAT EXCHANGERS (HX) USING ADVANCED MANUFACTURING (AM)

A Thesis

by

ASHOK THYAGARAJAN

Submitted to the Office of Graduate and Professional Studies of
Texas A&M University
in partial fulfillment of the requirements for the degree of

MASTER OF SCIENCE

Chair of Committee,	Debjyoti Banerjee
Committee Members,	Michael Pate
	Hadi Nasrabadi
Head of Department,	Andreas A.Polycarpou

December 2019

Major Subject: Mechanical Engineering

ABSTRACT

The largest consumer of fresh water from natural resources in the US currently are the industrial cooling towers devoted to thermal power generation (for cooling of steam from turbine exhaust). As the energy demands are on the rise, the availability of water for the cooling purposes would be insufficient in the years to come. With increasing population eventually the fresh water resources will be stressed to capacity (both for meeting the increased human consumption as well as for addressing the increasing energy needs of the growing population). As a result, alternate technologies are needed to wean power plants from using fresh water resources. Dry cooling using air cooled heat exchangers is an alternative to wet cooling (i.e., by obviating cooling towers). However, this option results in reduced operational efficiency, higher costs (both for capital costs and operating costs) and reduced operational reliability. Air cooled heat exchangers installed in arid climates are inoperable on certain days during summer as the ambient air temperature can exceed the temperature of the steam at the turbine exhaust and may lead to power plant shutdown, in-turn, causing instability in the electric supply grid infrastructure (thus compromising reliability). In order to combat these shortcomings, supplemental cooling options may be needed. Thermal Energy Storage (TES) platforms can provide an attractive option for supplemental cooling. Phase Change Materials (PCM) are often used as viable options for Latent Heat Thermal Energy Storage Systems (LHTESS) as they have small footprint owing to the high latent heat values of PCM.

The objective of this study is to analyze the performance of various LHTESS platforms by utilizing different configurations of the Heat Exchangers (HX) that are filled with PCM. The scope of this study is limited to using an organic Phase Change Material (PCM) and two different HX configurations are explored in this study: (a) two Shell and Tube Heat Exchangers that were

fabricated using Advanced Manufacturing (AM) technique (i.e., “3D Printing”); and (b) a conventional Chevron Plate Heat Exchanger (PHX) that was procured commercially from a vendor. The thermal response and performance characteristics (e.g., power rating and HX effectiveness) of the two HX configurations are measured experimentally in order to ascertain their efficacy for melting and solidification of the PCM for different flow rates and inlet temperature values of the working fluid. The working fluid is called the Heat Transfer Fluid (HTF). The HTF used in this study is tap water. The PCM used in this study is PureTemp 29 (commercially procured from Pure Temp Inc., Minneapolis, MN).

The propagation of the melt and the freeze fronts were monitored and tracked based on the nature of the transient temperature profiles recorded by an array of thermocouples. The array of thermocouples were strategically mounted at different locations within the HX containing the PCM. For the 3D-Printed HX (Shell and Tube HX), the thermocouples were located at different radial and axial locations within the shell containing the PCM. For the PHX, the thermocouples were located at different heights (for different plates containing the PCM). The transient values of the power and capacity ratings for the HX were estimated based on the time-history of the transient values of the temperature differential for the bulk temperature of the HTF flowing between inlet and outlet ports of the HX (and this was correlated with the transient profile and location as well as the propagation of the solid-liquid interface within the HX).

The performance characteristics of both HX, analyzed from the experimental data, show that the average power rating for the melting-cycle is consistently higher than that of the solidification-cycle due to the dominance of free convection during melting (resulting in higher values of the effective heat transfer coefficients for the same temperature differential values); while the

solidification process is dominated by transient conduction (resulting in lower values of the effective heat transfer coefficients for the same temperature differential values).

ACKNOWLEDGEMENT

I would like to thank my committee chair, Dr. Debjyoti Banerjee, and my committee members, Dr. Michael Pate and Dr. Hadi Nasrabadi, for their guidance and support during the course of this research. I am grateful to the constant love, support and encouragement provided by my father and mother. I also extend my thanks to all my friends and family, colleagues at the Multi Phase Flow and Heat Transfer Laboratory, faculty and staff of the Department of Mechanical Engineering at Texas A&M University, College Station for making my learning experience an enjoyable one.

Many thanks to Dr. Navin Kumar, Mr. Reynaldo Chavez and Mr. Lucas Nesbitt for their assistance with fabricating the 3D printed heat exchangers that I used for performing the experiments.

CONTRIBUTORS AND FUNDING SOURCES

Contributors

This work was supervised by a thesis committee consisting of Professor Debjyoti Banerjee (advisor) and Professor Michael Pate of the Department of Mechanical Engineering and Professor Hadi Nasrabadi of the Department of Petroleum Engineering.

All other work conducted for the thesis was completed by the student independently.

Funding Sources

This work was supported in part by the Department of Energy (DOE), Advanced Research Project Agency-Energy (ARPA-E) and T3 Texas A&M Triads for Transformation.

Its contents are solely the responsibility of the author and do not necessarily represent the official views of the Department of Energy or Texas A&M University.

NOMENCLATURE

c_p	Specific heat (J/kg-K)
E	Energy
HTF	Heat Transfer Fluid
h_{fs}	Latent heat of fusion
LHTESS	Latent Heat Thermal Energy Storage System
LHTS	Latent Heat Thermal Storage
m	Mass
$\dot{m}$	Mass flowrate
P	Power
PCM	Phase Change Material
LHSU	Latent Heat Storage Unit
Pr	Prandtl Number
Re	Reynold's Number
TES	Thermal Energy Storage
T	Temperature
ΔT_{HTF}	Temperature gain or loss by the HTF
u	Measurement uncertainty
$\dot{V}$	Volumetric flow rate
GPH	Gallons per hour
φ	Diameter

Greek symbols

ε	Effectiveness
ρ	Density

Subscripts

avg	Average

TABLE OF CONTENTS

LIST OF FIGURES

LIST OF TABLES

CHAPTER 1

INTRODUCTION

1.1 Phase Change Materials

In conventional lexicon, the term Phase Change Materials (PCM) is used to refer to a class of materials that possess “high” values of latent heat (i.e., phase change enthalpy). PCM are typically selected for enabling Thermal Energy Storage (TES) in smaller form factors. This type of TES platforms are therefore termed as Latent Heat Storage Units (LHSU). While there are several types of PCM that are used for typical commercial TES applications, and the conventional applications of PCM involve solid-liquid phase transition phenomena. Figure 1 shows the classification of different types of Thermal Energy Storage (TES) platforms, categorized based on the nature of material interactions in the storage media.

Phase transition from solid to liquid (melting process) occurs when PCM are subjected to a temperature above the melting point. During the melting process, the transfer of energy from the surroundings causes the internal energy of the molecules of PCM to rise eventually leading to the dissociation of the inter-molecular bonds. This dissociation of bonds is accompanied by a deviation from ordered physical structure of the molecules in the material, thus forming a distinctly discernible liquid phase.

During the reverse process (solidification), the liquid PCM must be subjected to a temperature lower than that of the phase transition temperature (freezing point), and this temperature differential is referred to as the degree of subcooling (that is required to initiate the solidification process within a melt pool).

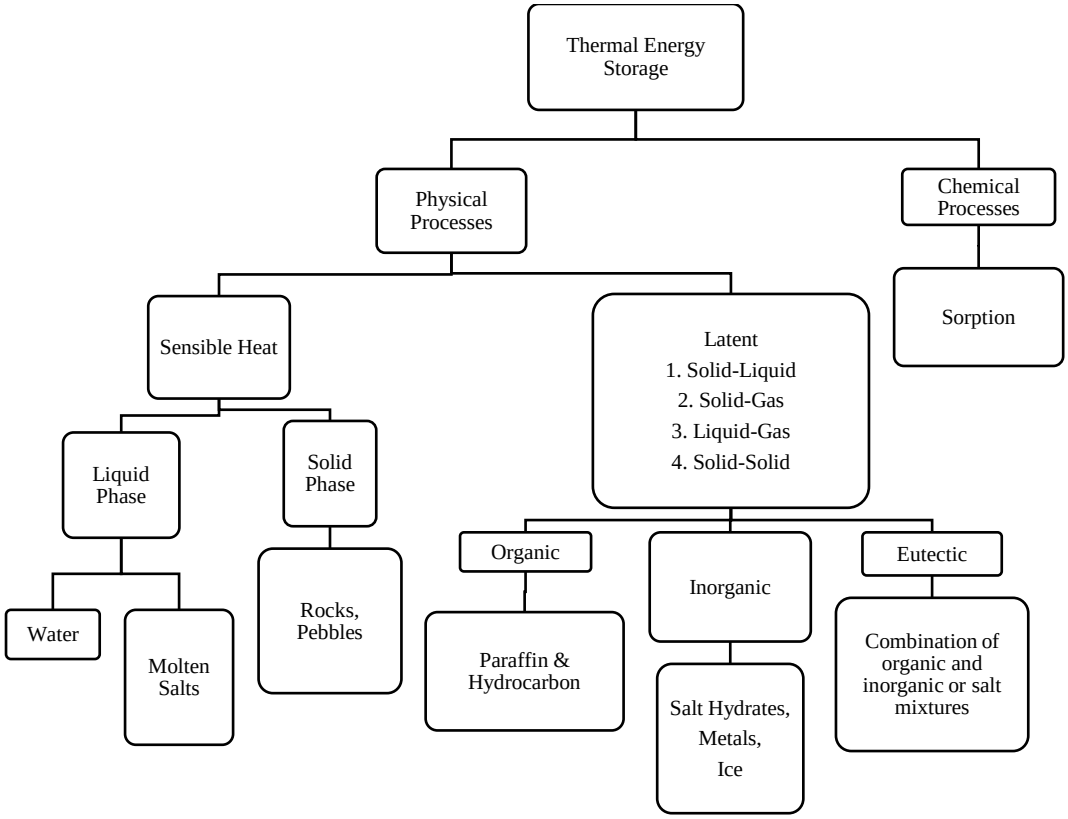

Figure 1. Classification of different types of thermal energy storage (TES) materials (Kumar N. 2018)

In this process, the PCM sample transfers thermal energy to the surroundings thereby leading to a reduction in the internal energy of the molecules and eventual reordering of the molecules to form a distinctly discernible solid phase. Even though, the thermal energy storage in Phase Change Materials (PCM) is dominated by latent heat storage in most applications, a certain degree of sensible heat storage in both solid and liquid phase is typical in engineering applications (but typically comprises of a negligible fraction of the total energy stored in the TES platform). As shown in Figure 2, during the melting or freezing process, the local temperature of the PCM in the

vicinity of the solid-liquid interface is isothermal, corresponding to the phase transition temperature of the material.

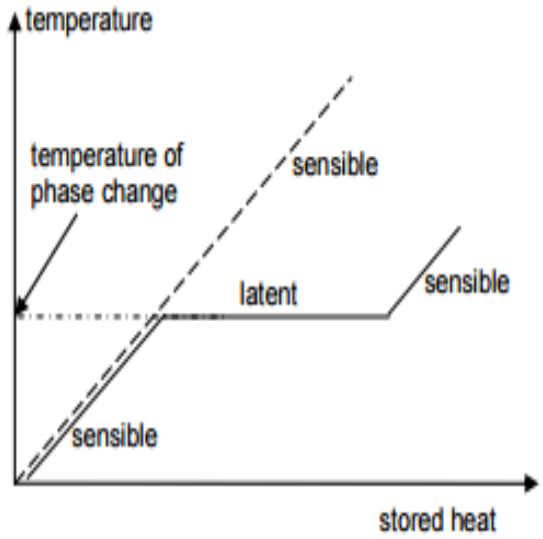

Figure 2 Phase Change Process (Kumar N. 2018)

1.2 Classification of Phase Change Materials

Phase Change Materials (PCM) are commonly classified as organic, inorganic and eutectics (A.Abhat 1983) (G. Lane 1983) and (Dincer 2002). There are advantages and disadvantages associated with each PCM. Additional information on PCM can be found in (F.A.Kulacki 2018) (Banerjee 2013) (B. Zalba 2003) (A. Sharma 2009). The table below lists the advantages and disadvantages accruing from the selection of different types of PCM.

A. Organic PCM:

Organic PCM usually leverage covalent bonding and are typically sourced commercially from agricultural/ food processing industries. One of the important advantages of organic PCM is that they have congruent melting and have high thermal stability (thus offering more reliable options at the expense of lower performance ratings, compared to that of the inorganic PCMs). It is due to this high thermal stability that organic PCM has been widely used in several engineering and commercial applications. Another major advantage of using organic PCM is they are not susceptible to phase segregation and are not corrosive (unlike inorganic PCM, which suffer from material compatibility issues as they are often highly corrosive to a variety of metals and alloys). The low corrosive property of organic PCM accrue from their chemical properties since they are typically composed of long chain hydrocarbons (n-alkane) which are not reactive to metals and alloys. Most of the organic PCM are also characterized by the absence of a distinct melting and solidification temperature – since the organic PCMs are often composed of a mixture of hydrocarbon derivatives and therefore undergo phase transition over a narrow range of temperatures.

Organic PCMs are typically available in the form of paraffin waxes (with different values of molecular weights), alcohols, glycols, esters, etc. The melting point of the PCM depends on the length of the carbon chain (as well as their chemical structures, e.g., straight chain versus branched chain structures, aliphatic versus aromatic, etc.). However, non-paraffin based PCM have lower melting points in general and are more suitable for low temperature applications. The major drawback of using organic PCM is the low thermal conductivity and low energy storage density in comparison to that of the inorganic PCM. Table 2 provides a list of the typical values of the material properties of conventional organic PCMs.

Table 1 Classification of PCM (Kumar N. 2018)

	Organic PCM	Inorganic PCM	Eutectics
Advantages	Non-corrosive	High Storage Density	Congruent melting point of elements
	High thermal stability	High Thermal Conductivity	High energy storage density
	No phase segregation		
Disadvantages	Flammable	Corrosive	Lack of an extensive property database
	Low Thermal Conductivity	Lack of thermal stability in pure form	
	Low Storage Density	Phase segregation	

B. Inorganic PCM:

In contrast to the covalent bonding typically encountered in organic PCM, ionic bonding is a characteristic of inorganic PCM. Commonly used inorganic PCM include alkali metal salts, salt hydrates, etc. In comparison to the organic PCM, inorganic PCM have a greater energy storage density, high thermal conductivity and have wider phase transition temperatures depending on the composition of the salt. The higher latent heat values associated with salt hydrates are attributed to the greater bond energy associated with the ionic bonds.

Most salt hydrates used as PCM have a stable crystal structure and are formed by the addition of stoichiometric quantities water to the anhydrous salt samples. They provide a wide range of options for selection of PCM for different applications with melting points varying from 30 °C to 150 °C. Due to their higher thermal conductivity, high values of thermal energy storage density and wider range of phase transition temperatures, inorganic PCMs offer a wider range of options that are suitable for applications in a variety of fields. However, unlike organic PCM, they are corrosive, often suffer from debilitating effects of phase segregation during melting and typically require increasing magnitudes of subcooling to initiate the solidification process (with each cycle during repeated melting and freezing cycles). A detailed review on current status and challenges of inorganic PCMs in LHTESS is given in (M. A. Shamseldin 2017). There are several methods reported in the literature to promote nucleation and reduce subcooling such as seeding (using additives) or adopting dynamic nucleation techniques such as cold fingering technique, use of high pressure and shock waves, etc. (E. Gunther 2007). The degree of subcooling for some of the conventionally used inorganic PCM and the additives used to reduce the degree of subcooling can be found in (B. C. Shin 1989), (O'Malley 2015), (Gawron 1980), (Kai 1984), (G. A. Lane 1992), (H. W. Ryu 1992), (M. M. Farid 2004), (L. F. Cabeza 2003), (B. G. Ramirez 2014), (Abhat 1981), (Schroder 1980), (Danilin 1981) and (Rossow 1979). Table 3 provides a list of the thermo-physical properties of a few conventional inorganic PCM.

Table 2 Thermo-physical properties of conventional organic PCMs

Material	Type	Melting temperature [° C]	Melting enthalpy [kJ/kg]	Thermal conductivity [W/ (m.K)]
Heptadecane	Paraffin	19	240	0.21 (solid)
Octadecane	Paraffin	28	245	0.358 (solid)
				0.148 (liquid)
Polyethylene	Paraffin	35	200	–
Caprylic acid	Fatty	16	149	0.149 (liquid)
Lauric acid	Fatty	42	178	0.147 (liquid)
Palmitic acid	Fatty	61	185	–

Table 3 Thermo-physical properties of conventional inorganic PCMs

Material	Type	Transition Temperature [°C]	Melting Enthalpy [kJ/kg]	Thermal Conductivity [W/ (m. K)]
$LiNO_3$	Salt	245	360	0.58 (liquid)
				1.37 (solid)
KNO_3	Salt	333	266	0.5 (liquid)
$MgCl_2$	Salt	714	266	–
KF	Salt	857	452	–
KF $3H_2O$	Salt	18.5	231	–
	Hydrate			
$CaCl_2$ $6H_2O$	Salt	30	190	0.54 (liquid)
	Hydrate			1.088 (solid)
Na_2HPO_4 $12H_2O$	Salt	35	280	0.476 (liquid)
	Hydrate			0.514 (solid)
$MgCl_2$ $6H_2O$	Salt	117	169	0.57 (liquid)
	Hydrate			0.704 (solid)

1.3 Phase Change Materials for Supplemental Cooling

The largest consumer of fresh water from natural resources in the US currently are the industrial cooling towers devoted to thermal power generation (for cooling of steam from turbine exhaust). As the energy demands are on the rise, the availability of water for the cooling purposes would be insufficient in the years to come. With increasing population eventually, the fresh water resources will be stressed to capacity (both for meeting the increased human consumption as well as for addressing the increasing energy needs of the growing population). As a result, alternate technologies are needed to wean power plants from using fresh water resources. Dry cooling using air cooled heat exchangers is an alternative to wet cooling (i.e., by obviating cooling towers). However, this option results in reduced operational efficiency, higher costs (both for capital costs and operating costs) and reduced operational reliability. Air cooled heat exchangers installed in arid climates are inoperable on certain days during summer as the ambient air temperature can exceed the temperature of the steam at the turbine exhaust and may lead to power plant shutdown, in-turn, causing instability in the electric supply grid infrastructure (thus compromising reliability). In order to combat these shortcomings, supplemental cooling options may be needed. Thermal Energy Storage (TES) platforms can provide an attractive option for supplemental cooling. Phase Change Materials (PCM) are often used as viable options for Latent Heat Thermal Energy Storage Systems (LHTESS) as they have small footprint owing to the high latent heat values of PCM.

Thermoelectric power generation is the largest consumer of fresh water resources in the United States, consuming 139 billion gallons of water in a single day of which roughly 4.3 billion gallons of water per day are lost in the form of evaporation to the environment (Simmons 2013). Also, the efficiency of thermoelectric power plants are typically in the range of 35~55% (K. Birkinshaw

2002) which implies that the heat rejection from power plants can be deleterious to the water bodies as the rejection of several megawatts of heat from power plants lead to runaway thermal pollution, thus enhancing the risk of potentially endangering the local eco-systems.

Since wet cooling involves water supplied from cooling towers, the heat exchangers tend to be more efficient and compact, due to the higher values of the specific heat capacity of water and the larger magnitudes of overall heat transfer coefficient in liquid-liquid heat exchangers (compared to that of the air-cooled heat exchangers), thus reducing both capital costs and operational costs, yielding more economically favorable options. Hence, almost 99% of the thermal power plants employ wet cooling (Kumar 2018). However, over-dependence on traditional wet cooling technologies is not sustainable in the long-run and thus, enhancement of dry cooling technologies are necessary to improve both performance and reliability of the air cooled power generation systems. Hence, to overcome the inherent drawbacks of air-cooled heat exchangers, Latent Heat Thermal Energy Storage Systems (LHTESS) that typically leverage PCM based heat exchangers, can provide cost-effective options for supplemental cooling for the traditional dry power generation.

In particular, LHTESS can be used for providing supplemental cooling to combat the inefficiencies endemic in dry cooled platforms (that were specifically developed for power generation in arid regions where the ambient temperature escalates significantly during the day, thereby exerting significant backpressure on the turbine and, in turn, can cause tripping failure in power plants).

1.4 Literature Review on PCM LHTESS

In literature, the most commonly used Heat Exchanger configuration for LHTESS is the Shell and Tube Heat Exchanger because of the lower cost and operational efficiencies associated with these platforms (e.g., lower pressure penalty for the same power rating). Gong and Mujumder (Gong 1997) investigated the effect of flow direction of the HTF on the thermal performance of PCM based TES. Experiments were conducted with CaF_2 as PCM and He/Xe mixture as the HTF. They concluded that the parallel flow arrangement provided 5% higher power rating than the counter flow arrangement with HTF entering at opposite ends for charging and discharging cycles. This result was attributed to the higher temperature difference between inlet HTF and PCM during both the cycles. Additionally, the counter flow arrangement also produced significant supercooling of the PCM at the inlet.

Rathod and Banerjee (M.K. Rathod 2014) conducted experiments on a vertical concentric tube heat exchanger with paraffin wax as PCM and water as HTF. Experiments were conducted to examine the effect of HTF mass flow rate and inlet temperature for the cycle. During melting, for a constant HTF inlet temperature of 85°C, increasing the mass flow rate from 1 kg/min to 4 kg/min increases the Reynolds number from 1709 to 6835, which in turn, reduces the melting time by 19%. A stronger influence of inlet temperature on the melting time was observed when the inlet temperature was varied from 75°C to 85°C at a constant mass flow rate of 5 kg/min. Melting time was reduced by 44% as the inlet temperature was increased. The authors cited the enhancement of natural convection due to higher temperature difference between the HTF and PCM, thus yielding significant reduction in melting time (and therefore, higher power rating during melting). However, the authors neglected to mention the actual time required for the solidification-cycle,

possibly due to the lower power rating caused by the dominance of conduction heat transfer (over natural convection or mixed convection) during solidification.

Hosseini et al (M. Hosseini, Experimental and computational evolution of a shell and tube heat exchanger as a PCM thermal storage system 2014) conducted similar experiments to determine the impact of inlet temperature on the thermal performance of a horizontal double pipe heat exchanger. Commercially sourced samples of paraffin wax (RT 50) was used as the PCM in the shell side of the heat exchanger and had a total weight of 4 kg. Water was used as the HTF at a constant flow rate of 1 L/min with inlet temperature varying from 70°C to 80°C. They reported that the increase in the inlet temperature leads to a shorter melting time, reducing it by 19% and 37%, as the inlet temperature was increased in steps of 5°C from the base temperature of 70°C.

Agarwal and Sarviya (Sarviya 2016) conducted experiments on a horizontal double pipe heat exchanger that was filled with paraffin wax (as PCM) in the annular space. The inlet temperature of HTF was varied between 80°C to 90°C while the mass flow rate was maintained at 3kg/s. The melting time was set to 8 hours as the experiment was designed to explore the application of LHTESS to a solar dryer. The authors reported a reduction in the melting time of 9% and 16% as the inlet temperature was increased from 80°C to 90°C. The effect of mass flow rate was explored during solidification by varying the mass flow rate of the heat exchanger (1.5 g/s, 2.2 g/s, 3 g/s) at a constant HTF temperature of 30°C. The authors reported an increase in the solidification time by 13% and 23%, as the mass flow rate was decreased to 2.2 g/s and 1.5 g/s respectively from 3 g/s.

Avci and Yazici (Yazici 2013) conducted similar experiments on a horizontal double pipe heat exchanger with PCM PF56-58 in the annulus of the heat exchanger. The inlet temperature of the

HTF was varied from 75°C, 80°C and 90°C with a constant mass flow rate of 280 kg/hr. As reported by previous studies, the melting time was reduced significantly as the inlet temperature of the HTF was increased. The authors also confirmed the propagation of the melt front from the top of the heat exchanger radially inwards during charging. However, during discharging, the melt front moved radially outward after forming a thin layer of solid PCM around the tube. As expected, the solidification time decreased as the inlet temperature of the HTF was lowered, as greater thermal gradients enhanced the heat transfer from the HTF to the PCM.

Effect of the inclination angle of the Heat Exchanger was explored by Koshua et al. (N. Kousha 2017) using a double pipe heat exchanger at inclination angles of 0°, 30°, 60° and 90° (with respect to the horizontal plane). The shell side of the PCM was filled with paraffin wax (RT 35), with water as the HTF. The HTF flow rate was fixed at 400 ml/min. The inlet temperatures were varied between 70°C to 80°C. The authors reported that the melting process was faster when the heat exchanger was fixed horizontally while the solidification time was aided by the vertical orientation. As pointed out in previous studies, increasing inlet temperature impacted the charging process significantly.

Saddegh et al (S. Seddegh 2017), performed experiments on a vertical double pipe heat exchanger with a large shell of outer diameter of 0.35 m and 0.5 m height (48.11 L capacity) and this apparatus was filled with 25 kg of PCM (RT 60). Water flowed through the inner pipe of diameter 0.02 m (consisting of DN20 copper pipe) at a fixed flow rate of 10 L/min and at fixed inlet temperature values of either 80°C or 10°C, respectively. The authors used a transparent polypropylene shell for visual observation of the geometric profile of the solid-liquid interface and the propagation of the melt front during thermo-cycling. However, the lack of insulation led to heat loss from the

shell during the experiments. From the experiments, the authors concluded that the melt front propagates in a conical manner from the top of the heat exchanger to the bottom until right before the liquid PCM fills the shell completely. This result, therefore, contradicted the previous study by Joybari and Haghighat, (M. M. Joybari 2016) and Joybari et al (M. M. Joybari 2017), who proposed that the melt front propagates radially outward from the pipe in a cylindrical manner. This observation combined with the higher temperature readings from the axial thermocouples at the top of the heat exchanger led the authors to confirm that natural convection dominated the heat transfer mechanism during melting, which in turn were proposed by Akgün et al (Akgün, Experimental study on melting/solidification characteristics of a paraffin as PCM. Energy Conversion and Management 2007) (Akgün, Thermal energy storage performance of paraffin in a novel tube-in-shell system 2008), Longeon et al (Longeon 2013), Murray & Groulx (Murray 2014) and Trp (Trp 2005). The experimental validation of numerical predictions confirmed the presence of both axial and radial convection currents within the HX (e.g., by using velocity vector plots for the PCM within the shell of the HX). The authors further confirmed the presence of a thin confinement layer of melted PCM that existed throughout the melting process and which did not increase in thickness, even though conventional wisdom would have predicted the anomalous transport of the melted PCM, solely, by vertical free convection. During solidification cycle, the authors observed the propagation of solidification front from the bottom of the heat exchanger as it progressed both in radial and axial directions. Similar to the melting process, the solid phase of the liquid PCM was transported by free convection and the presence of cooler liquid at the bottom ensured that the bottom portion of the heat exchanger solidified first in the experiments.

Garcia-Alonso (J. García-Alonso 2014) conducted experiments using a Shell and Tube Heat Exchanger with salt hydrate PCM encapsulated inside 24 tubes that were confined using baffles. The stainless steel shell was insulated with an elastomer blanket. Since, the application was driven towards radiant floor heating and domestic hot water production, the PCM was melted using a ground source heat pump that maintained the water inlet temperature at 50°C while during the solidification process, the water inlet temperature was fixed at 20°C. The flow rate of the fan coil was varied to the following values: 160 m^3/hr, 250 m^3/hr and 390 m^3/hr. The authors concluded that the magnitude of the heat transfer within the PCM encapsulations were negligible compared to that of the radial direction.

Tao et al (Y. Tao 2017) performed numerical simulations to study the performance of a double pipe heat exchanger with PCM in the shell side (Model A) and tube side (Model B). The inlet flow condition of the He/Xe HTF was the same for both the arrangements and the amount of PCM was kept constant by varying the dimension of the pipe in both models. A 1D fluid flow model was used for the HTF neglecting the axial conduction and viscous dissipation. A 3D model was used for the PCM and the effect of natural convection was analyzed. The authors reported that for the tube arrangement, during charging, both the latent heat storage rate and melting time were enhanced with PCM on the tube side with further enhancement caused by natural convection. The authors, however, noted that the effect of natural convection can be discarded during the discharging process. Based on the predictions from their numerical simulations, the authors suggested using a tube model for practical applications.

Pirasaci and Goswami (Goswami 2016) focused on the design of a latent heat storage unit for direct steam generation power plants. They based their simulations on a shell and tube heat

exchanger with NaCl-$MgCl_2$ eutectic PCM that was used to superheat the feed water from 380 °C to 580 °C. The authors used effectiveness as the design criterion and considered several design parameters such as length of the storage unit, flow rate of HTF, diameter of the tubes and the distance between the tubes to study their impact on the performance. Based on their results, the authors suggested that increasing the length of the storage unit increases the effectiveness. Similarly, smaller diameter tubes were also predicted to increase the effectiveness. However, since smaller tubes cause higher pressure losses the authors suggested that an optimal diameter needs to be identified in order to optimize the effectiveness of the HX. The authors also pointed out that there is an optimal Reynolds number of 1271 per tube that improves the performance of the storage unit.

Rasta et al (I.M. Rasta 2018) propose the use of vegetable oil esters and water mixtures as biologically derived PCMs ("Bio-PCM") for subzero energy storage in a refrigeration cycle. Based on the experimental results the authors concluded that the use of vegetable oil esters as PCM reduces the degree of the subcooling (compared to that of regular tap and mineral water).

The degree of subcooling was also lower than that of the traditionally used additives such as propylene glycol. This is specifically beneficial in refrigeration cycles as the coefficient of performance of the refrigeration system depends on the evaporator temperature. When using tap water as PCM, the subcooling can be high reducing the evaporator temperature and hence affecting the COP. Based on the results reported by the authors, the use of vegetable oil esters completely eliminated subcooling and enhanced the reliability.

Based on these literature reports it is apparent that enhancement of heat transfer coefficients (both overall heat transfer coefficient as well as the heat transfer during solidification of PCM) are key to enhancing the performance of PCM based LHTESS. This is discussed in the next section.

1.4.1 Heat Transfer Enhancement Techniques

Hosseini et al. (M. Hosseini, Thermal analysis of PCM containing heat exchanger enhanced with normal annular fins p 2015) conducted experiments on a double pipe heat exchanger with 8 circular, symmetric and equally spaced fins normal to the pipe axis. Three sets of sensor-arrays were mounted along the axis (two adjacent to fins and one on the mid-section) for recording temperature profiles within the PCM, i.e., by using a total of 16 thermocouples for obtaining the measurements of temperature (at two radial locations, at 12.5mm and 32.5 mm from the pipe) and at varying angular positions. Two different fin heights (13 mm and 26 mm) and three different Stefan Numbers (0.26, 0.28, and 0.32) were selected for the study. Based on the experimental data, the authors concluded that melting occurs first on the portion above the pipe followed by the lateral portion of the shell. Using numerical simulations, the authors predicted the propagation of the melt front in the shell and identified that the taller fins led to shorter melt times since the larger radial penetration of the fins within the PCM caused an enhancement of the heat transfer rates. The melt propagation itself was faster closer to the fins than the midsection (where the fins were not positioned in close proximity). The authors also pointed out that the increase in the height of the fins reduced the melt time by 19%. Increasing the Stefan Number also reduced the melt time by 20% and 38% for the 13 mm fin while it reduced the melt time by 15% and 28% for the 26 mm fin. During solidification, the authors predicted that the Stefan Number did not impact the process

time as much as it did for melting even though, the total solidification time was reduced by 16% for the taller fin.

Shon et al (J. Shon 2014) explored the application of finned compact heat exchanger in the recovery of waste heat from the coolant from a hot engine. The stored heat was used to reduce the warm-up time during cold startup of the engine. Based on theoretical calculations, the authors performed their study for a commercially available heat storage system that had the volumetric capacity to store 4.2 kg of Solid Xylitol that was packed in this device (in place of commercially used coolant between the fins and tube of the heat exchanger). Noting that increasing both the mass flow rate of coolant inside the pipe and area of fins in contact with the liquid – the authors reported that Xylitol reduced the convective flow resistance of the coolant inside the tube (and also the convective resistance of the liquid PCM between the tube and un-melted – solid PCM). The authors based their predictions for a 100 tube HX (with 3 mm hydraulic diameter), with 250-fins (with fin dimension of 172 mm × 72 mm × 0.1 mm each). The authors observed that varying the inlet temperature of the coolant had significant effect on the melting rate of PCM while increasing the flow rate marginally accelerated the melting process. Based on the warm-up experiment conducted under idling conditions, the warm-up time in the PCM heat exchanger was reduced by 33.7% compared to that of the conventional heat exchanger. The authors also suggested using a PCM with low viscosity to enhance the convective heat transfer coefficient of the liquid PCM, in order to reduce its contribution to the overall thermal resistance in the representative thermal impedance network.

Medrano et al (M. Medrano 2009) conducted experiments to characterize the performance of small PCM storage systems during melting and solidification that are appropriately sized for domestic

applications and other small-scale systems. For all of the heat exchangers used in this study, PCM RT 35 with a melting point of 35 °C was used. Three sets of Double-Pipe HX were used in this study: one with copper tube and the rest with graphite matrix (and 13 radial copper fins) were used along with a compact heat exchanger with aluminium fins and gasketed plate heat exchangers. The authors noted that higher Reynold's number is desirable in turbulent flow regime as it reduces the time to complete the phase change process. Also, temperature difference values ranging from 15 °C to 25 °C was observed to decrease the time required for completing the phase change process by 30% to 60%, respectively. The authors also concluded that the simple double pipe heat exchanger and plate heat exchanger are inefficient for practical applications as they typically possess lower surface area that is available for heat transfer and also can house only lower quantities of PCM (thus compromising their net heat storage capacity). Among the other types of heat exchangers considered in this study, compact heat exchangers were reported to have the highest average thermal power rating. When considering the average thermal power per unit area and per unit thermal gradient, the double pipe heat exchanger with graphite matrix performed better than all of the heat exchangers explored in this study.

Ibrahim et al (N. I. Ibrahim 2017) presented a review on the recent developments in heat transfer enhancement techniques in Latent Heat Thermal Energy Storage Systems. From their review, they classified the heat transfer enhancement techniques into two broad classes: (a) heat transfer area based, and (b) thermal conductivity based. While fins and heat pipes were used to enhance the heat transfer area, high conductivity materials/ particles were used to enhance the thermal conductivity of the PCM. The authors pointed out the dearth of techniques that can simultaneously enhance

both heat transfer area and thermal conductivity. Hence the authors suggested more studies are needed to explore the efficacy of the proposed combined heat transfer enhancement techniques.

Amagour et al (M. E. H. Amagour 2018) performed experiments on a compact heat exchanger with rectangular fins and tube (made of aluminum) to study the effect of flow rate on the charging and discharging cycles for a fixed melting temperature of 80°C and cooling using ambient air. The performance of the heat exchanger was analyzed using the effectiveness-NTU method. Based on their findings, the authors concluded that high flow rates were not suitable for heat retrieval applications. They also noted that the higher flow rates accelerated the phase change process and reduced the average effectiveness of the system. According to the authors, the effectiveness was higher during solidification process (than that of the melting process) and that lower flow rates were desirable for enhancing the efficacy of the TES platform.

Based on the review on existing literature, there is limited data available on the melt and freeze front propagation in a single shell multiple tube heat exchanger. Additionally, comparison on the effect of heat exchanger type on performance is also insufficient. Thus, this study is aimed at addressing the voids identified in the available literature on the use of latent heat thermal energy storage systems (LHTESS) for supplemental cooling.

1.5 Motivation and Goals

The motivation of this study is to explore the thermal performance of technologies that utilize latent heat thermal energy storage systems (LHTESS) for providing supplemental cooling in conventional dry cooling platforms, especially for mitigating water usage in thermal power generation systems. However, wet cooling based power generation systems are more efficient, economical and reliable; while dry-cooling based power generation systems are less efficient and are more costly with compromised reliability. Thus, the switch to dry cooling begs the integration with supplemental cooling systems that can enhance efficiency while also improving the operational reliability of the power generation systems. Hence, one of the goals of this study is to explore the performance of LHTESS that can potentially be used to for supplemental cooling with the aim of obviating water usage in cooling of thermal power generation units.

Apart from exploring the performance characteristics of different configurations of heat exchangers, propagation of melt and freeze fronts are determined experimentally from spatial temperature data over the duration of each duty cycle. The goal of this experiment is to provide experimental data that can be validated by computational fluid dynamics (CFD) simulations. Additionally, machine learning could be implemented to predict the propagation of melt and freeze fronts based on an extensive training data set. Although this may not be relevant to most organic PCMs (used in the study), prediction of melt propagation in LHTESS with salt hydrates as PCM is novel and extremely useful as it could potentially be used to improve the effectiveness of the "cold fingering" technique (a dynamic nucleation technique for creating a cold spot in the vicinity of the PCM sample such that a portion of the sample is always in solid state. It is commonly used to alleviate the effect of subcooling in inorganic PCM).

1.6 Objectives

The objective of this study is to perform experiments using a commercially procured Plate Heat Exchanger (PHX) and a 3D Printed Shell and Tube Heat Exchanger for comparing and contrasting their efficacy as Thermal Energy Storage (TES) platforms. The study was performed with the aim of monitoring the location and propagation of the solid-liquid interface within the PCM during both melting and freezing. The performance rating of the heat exchangers were determined based on the average power rating and HX effectiveness (as LHTESS).

The following are the main objectives of this study:

- Perform experiments to study the impact of variations in flowrate and inlet temperature on the rate of melting and solidification using three heat exchangers (PHX and two 3D printed shell and tube heat exchanger).
- Study the rate of propagation of the solid-liquid interface during both melting and solidification cycles by monitoring temperature measurements recorded using strategically mounted array of thermocouples within the PCM.

1.7 Scope

The aim of the study is to investigate the thermal performance characteristics of a commercially available PHX and a 3D printed shell and tube heat exchanger. The scope of the experiments is limited to an organic PCM (PureTemp 29 was selected for these experiments). The HTF inlet temperatures were limited to a range spanning from 20°C to 40°C (which is consistent with the supplemental cooling needs for thermal power plants in arid regions, as specified by the ARPA-E ARID program). As a result, the inlet temperature values of the HTF during melting were set to 37°C, 35°C and 33°C for the shell and tube heat exchanger, For the PHX, the inlet temperature values of the HTF during melting were set to 38 °C, 34 °C and 32 °C. The inlet temperature of HTF during solidification was set at 25°C for the shell and tube heat exchanger. For the PHX, the inlet temperature of HTF during solidification was set 20°C, 24°C and 26°C.

The propagation of the solid-liquid interface during melting and freezing were monitored only for the 3D printed shell and tube heat exchanger placed in a horizontal orientation. The radial temperature readings were obtained at distance of 16 mm, 12 mm, 8 mm and 4 mm from the inner wall of the 3D printed shell. Along the axis, temperatures were recorded at 100 mm, 155 mm and 190 mm from the inlet tube for the HTF. Organic PCM (PureTemp 29) utilized in this study has a melting temperature of ~29°C. The selection of PCM is guided by the nature of the application, reliability, desired storage capacity and the duration of the melting and solidification cycles.

CHAPTER 2

EXPERIMENTAL METHODS

2.1 3D Printed Shell and Tube Heat Exchanger (single point PCM temperature measurement)

2.1.1 Experimental Setup

The 3D solid model shown below in Figure 3 depicts the design and dimensions of the 3D printed Shell and Tube Heat Exchanger used in the study. The shell was 3D printed from a 3 mm filament ABS which has a thermal conductivity of ~ 0.1 [W/(m·K)]. A total of 12 stainless steel tubes were mounted inside the 3D printed Shell and Tube Heat Exchanger for exchanging heat between the PCM (placed in the shell) and HTF (flowing through the parallel array of tubes). Each Stainless Steel tube has an outer diameter of 0.25" and an inner diameter of 0.18". The length of each tube is measured to be 8" with a total effective HTF flow area of 0.164 cm^2.

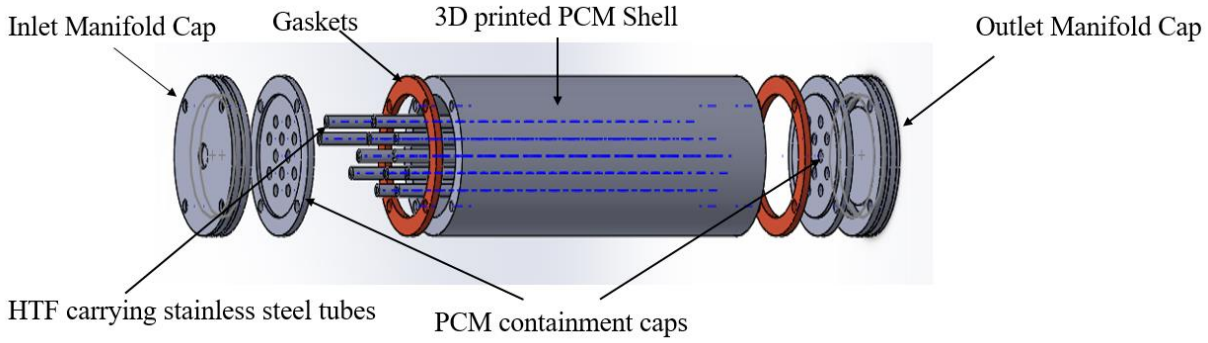

Figure 3. 3D model of the Shell and Tube Heat Exchanger (Single point temperature measurement)

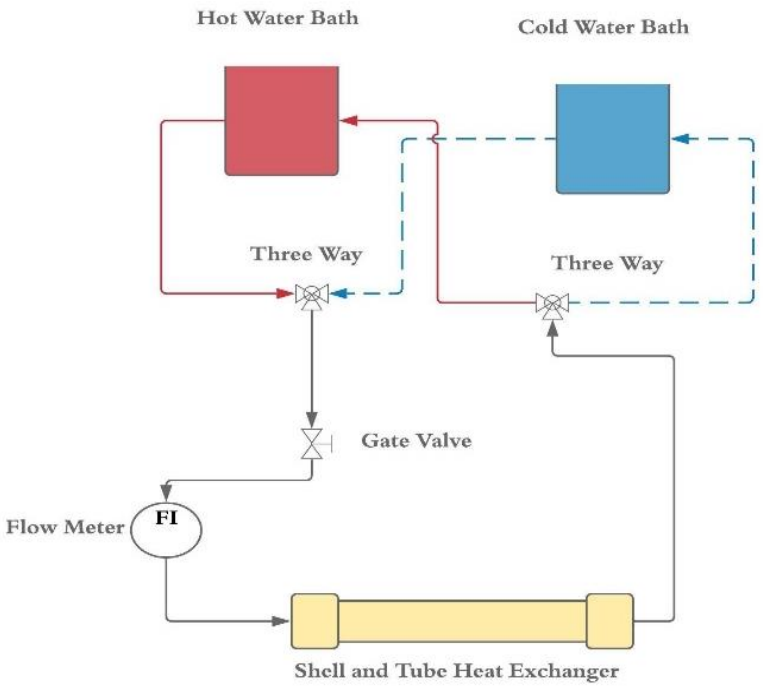

Figure 4. Schematic of the experimental setup for 3D Printed Shell and tube Heat Exchanger (Single point temperature measurement)

The shell was 3D printed using Lulzbot Taz 5 and the final dimensions of the shell is tabulated below.

Table 4 Dimensions of the 3D Printed Shell (Single point temperature measurement)

Dimension	Value
Height	8 inches
Diameter	3.25 inches
Wall Thickness	0.375 inches

Thermocouples used in this setup are wired "K" –type thermocouple (Omega, TT-K-24-SLE) with a measurement uncertainty of ± 0.35°C. The thermocouples were placed at the inlet and the outlet

of the Heat Exchanger to measure the change in the temperature of the Heat Transfer Fluid (Water). To measure the temperature of the PCM, the thermocouples were placed exactly at the center of the 3D Printed Shell. All the water lines from the water bath to the Heat Exchanger were insulated to minimize the heat loss to the environment. Temperature data was recorded using the NI SCXI 1000 Chassis and NI SCXI-1102 board at a sampling rate of 1 Hz.

HTF (water) is pumped into the Heat Exchanger from two constant temperature baths (Cole-Parmer StableTemp as the hot bath and VWR 1040 as the cold bath). A needle valve was used to vary the flow rate of the HTF and a flow meter (Omega FL-72 Series) was connected in series was used to measure the flow rate of the HTF. The vertical flowmeter has a precision uncertainty of ±0.5 GPH. The Phase Change Material selected for this study is organic PureTemp® 29 and the specifications of the PCM are provided below:

Table 5 Thermophysical Properties of PureTemp 29

Property	**Value**
Melting Point	29°C
Heat Storage Capacity	202 J/g
Thermal Conductivity (Liquid)	0.15 W/m°C
Thermal Conductivity (Solid)	0.25 W/m°C
Density (Liquid)	0.85 g/mL
Density (Solid)	0.94 g/mL
Specific Heat (Liquid)	1.94 J/g°C
Specific Heat (Solid)	1.77 J/g°C

It should be noted that the experimental values for the melting and solidification temperatures are 28.7°C and 22°C respectively (Kumar 2018). The difference in the melting and solidification is reported to be caused by thermal hysteresis in paraffin wax (L. Ying 2008) (S.Fleicher 2015). Thus, it can reasonably assumed that melting occurs in the temperature range of 20°C to 32°C and solidification occurs in the temperature range of 23°C to 17°C.

2.1.2 Experimental Procedure

Initially, water at 20°C from the cold water bath is supplied to the Heat Exchanger to initiate the solidification process after filling the 3D printed shell with a measured mass of melted PCM (0.454 g). Once the steady state conditions are attained, the valves are adjusted to supply water from the hot bath to initiate the melting process. The system is allowed to reach steady state before the valves are switched back to continue to repeat the next cycle. This procedure is repeated for varying volume flow rates and inlet temperature of the HTF. Each test condition is repeated thrice to record the statistical uncertainty for measuring the power rate and effectiveness of the HX. The test matrix for the experiment is tabulated below.

Table 6 Test Matrix for 3D Printed Shell and Tube heat Exchanger (single point temperature measurement)

Flow Rate (GPH)	Temperature Range (°C)
3	T_{hot} = 37/35/33
	T_{cold} =25
5	T_{hot} = 37/35/33
	T_{cold} =25
10	T_{hot} = 37/35/33
	T_{cold} =25

2.1.3 Data Reduction and Uncertainty Analysis

The following section discusses the data reduction and uncertainty analysis that was universally implemented for all the heat exchangers tested in this study.

The difference in the temperature between the inlet and outlet is given by

$$\Delta T_{HTF} = T_{outlet} - T_{inlet} \tag{2.1}$$

where, T_{outlet} is the HTF temperature measured at the outlet port of the heat exchanger and T_{inlet} is the inlet temperature measured at the inlet port of the heat exchanger.

The measurement uncertainty of ΔT_{HTF} is calculated as follows:

$$\boldsymbol{u_{\Delta T_{HTF}}} = \left[\left(\frac{\boldsymbol{\partial \Delta T_{HTF}}}{\boldsymbol{\partial T_{outlet}}}\right)^{\mathbf{2}} \left(\boldsymbol{u_{T_{out}}}\right)^{\mathbf{2}} + \left(\frac{\boldsymbol{\partial \Delta T_{HTF}}}{\boldsymbol{\partial T_{inlet}}}\right)^{\mathbf{2}} \left(\boldsymbol{u_{T_{inlet}}}\right)^{\mathbf{2}}\right]^{\mathbf{1/2}} \tag{2.2}$$

where, u is the measurement uncertainty for each variable: ΔT_{HTF},T_{out}, and T_{inlet} .

Effectiveness of the melting process is calculated by taking the ratio of the HTF temperature loss to the temperature difference between the inlet HTF temperatures to the average temperature of the PCM inside the heat exchanger.

$$\boldsymbol{\varepsilon_{melting}} = \frac{\boldsymbol{(T_{inlet} - T_{outlet})}}{\boldsymbol{(T_{inlet} - T_{PCM})}} \tag{2.3}$$

Effectiveness of the solidification process is calculated by taking the ratio of the HTF temperature gain to the temperature difference between the average temperatures of the PCM (inside the heat exchanger) to the inlet HTF temperature. This is shown in equation 2.4:

$$\boldsymbol{\varepsilon_{solidification}} = \frac{(\boldsymbol{T_{outlet} - T_{inlet}})}{(\boldsymbol{T_{PCM} - T_{inlet}})} \tag{2.4}$$

where, T_{PCM} is the average temperature of the PCM inside the plate heat exchanger, T_{inlet} is the HTF inlet temperature, and T_{outlet} is the HTF outlet temperature.

The uncertainty for the effectiveness is computed as shown:

$$\boldsymbol{u_{\varepsilon}} = \left[\left(\frac{\boldsymbol{\partial \varepsilon}}{\boldsymbol{\partial T_{inlet}}}\right)^{\boldsymbol{2}} \left(\boldsymbol{u_{T_{inlet}}}\right)^{\boldsymbol{2}} + \left(\frac{\boldsymbol{\partial \varepsilon}}{\boldsymbol{\partial T_{outlet}}}\right)^{\boldsymbol{2}} \left(\boldsymbol{u_{T_{outlet}}}\right)^{\boldsymbol{2}} + \left(\frac{\boldsymbol{\partial \varepsilon}}{\boldsymbol{\partial T_{PCM}}}\right)^{\boldsymbol{2}} \left(\boldsymbol{u_{T_{PCM}}}\right)^{\boldsymbol{2}}\right]^{\boldsymbol{1/2}} \tag{2.5}$$

where, u is the measurement uncertainty for each variable; ε, $u_{T_{out}}$, T_{PCM}, and T_{inlet} .

The specific heat capacity (C_p) of the HTF was calculated using the equation as shown below:

$$\boldsymbol{C_p} = \left[\boldsymbol{4 \times 10^{-13} T_{avg}^6 - 2 \times 10^{-10} T_{avg}^5 + 2 \times 10^{-8} T_{avg}^4 - 2 \times 10^{-6} T_{avg}^3 + 1 \times 10^{-4} T_{avg}^2 - 3.4 \times 10^{-3} T_{avg} + 4.2199}\right] \boldsymbol{1000} \tag{2.6}$$

The density (ρ) of the HTF was calculated as shown:

$$\boldsymbol{\rho} = \left[\boldsymbol{1 \times 10^{-7} T_{avg}^4 + 4 \times 10^{-5} T_{avg}^3 + 7.5 \times 10^{-3} T_{avg}^2 - 5.16 \times 10^{-2} T_{avg}}\right] + \boldsymbol{999.87} \tag{2.7}$$

The total energy storage for the melting process was obtained by numerical integration of the area between the inlet and outlet temperature plots of the heat transfer fluid (HTF). The mathematical formulation of the energy stored is expressed as:

$$\boldsymbol{E_T = \dot{m}_{water} C_{p,water} \int_{t=0}^{t=final} (T_{initial} - T_{final})\, dt} \tag{2.8}$$

where, $\int_{t=0}^{t=final}(T_{initial} - T_{final})\, dt$ is the numerical integral of the area under the ΔT_{HTF} curve, $C_{p_{water}}$ is the average specific heat capacity of water, and $\dot{m}_{water}$ is the average mass flow rate of the water to the heat exchanger.

The uncertainty in energy stored is calculated as follows:

$$\boldsymbol{u_E = \left[\left(\frac{\partial E}{\partial \dot{m}}\right)^2 (u_{\dot{m}})^2 + \left(\frac{\partial E}{\partial c_p}\right)^2 \left(u_{c_p}\right)^2 + \left(\frac{\partial E}{\int \partial \Delta T_{HTF}}\right)^2 (u_{\Delta T})^2 + \left(\frac{\partial E}{\partial t}\right)^2 (u_t)^2\right]^{1/2}} \tag{2.9}$$

where, t is time and u is the measurement uncertainty for each variable: $\dot{m}$, c_p, ΔT_{HTF} and t. For this experiment, u_{c_p} and u_t were considered to be negligible.

The uncertainty of the mass flow rate of the HTF is calculated as shown:

$$\boldsymbol{u_{\dot{m}} = \left[\left(\frac{\partial \dot{m}}{\partial \dot{V}}\right)^2 (u_{\dot{V}})^2 + \left(\frac{\partial \dot{m}}{\partial \rho}\right)^2 (u_\rho)^2\right]^{1/2}} \tag{2.10}$$

where, $\dot{V}$ is the measured volumetric flow rate of the HTF, ρ is the density of the HTF, $u_{\dot{V}}$ is the uncertainty for the volumetric flow rate and u_ρ is the uncertainty in the density. For this experiment, u_ρ and $u_{\dot{V}}$ were considered to be negligible.

The power rating for each trial is calculated as follows:

$$\boldsymbol{P_{avg}} = \frac{\boldsymbol{E_T}}{\boldsymbol{t_{melt/solid}}} \tag{2.11}$$

where, $\boldsymbol{E_T}$ is the experimental energy for the latent phase and $\boldsymbol{t_{melt/solid}}$ is the latent phase duration.

The uncertainty in the power rating of the heat exchanger is obtained as follows:

$$\boldsymbol{u_{P_{avg}}} = \left[\left(\frac{\boldsymbol{\partial P_{avg}}}{\boldsymbol{\partial E_T}}\right)^2 \left(\boldsymbol{u_{E_T}}\right)^2 + \left(\frac{\boldsymbol{\partial P_{avg}}}{\boldsymbol{\partial t_{melt/solid}}}\right)^2 \left(\boldsymbol{u_{t_{melt/solid}}}\right)^2\right]^{1/2} \tag{2.12}$$

where, $\boldsymbol{u_{E_T}}$ is the measurement uncertainty of the experimental energy stored and $\boldsymbol{u_{t_{melt/solid}}}$ is the uncertainty in the time. For this experiment, $\boldsymbol{u_{t_{melt/solid}}}$ is considered to be negligible.

2.2 Chevron Plate Heat Exchanger

2.2.1 Experimental Setup

The 3D solid model shown below in Figure 5 depicts the architecture of the Chevron Plate Heat Exchanger used in this study. The Chevron Plate Heat Exchanger used in this experiment has alternating layers of Phase Change Material (PCM) and flowing HTF (Water).

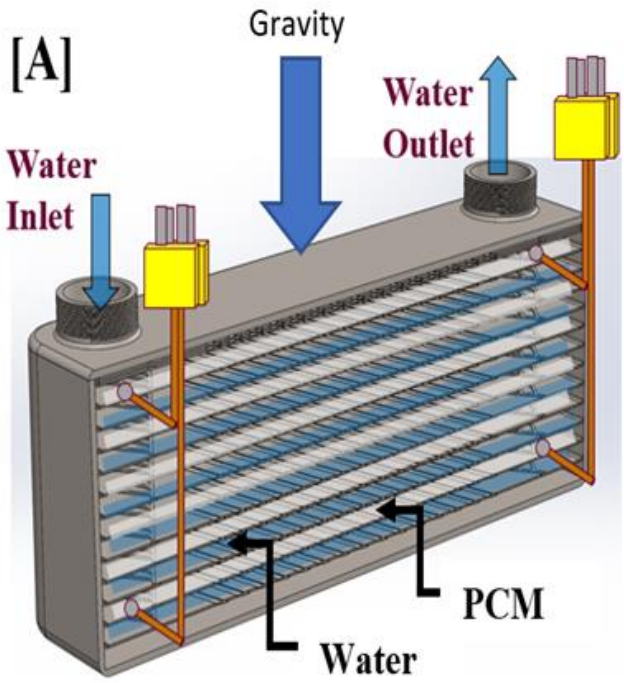

Figure 5 Cross Sectional View of Heat Exchanger highlighting the location of PCM, thermocouples and flow direction

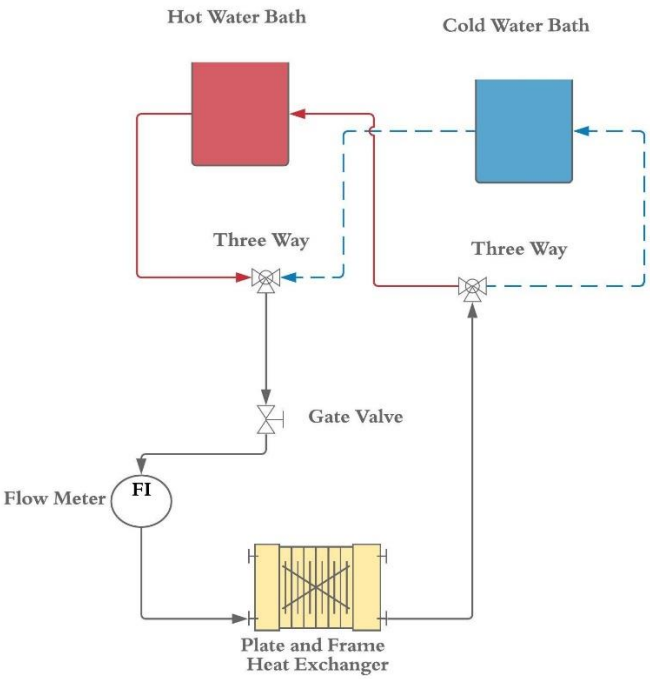

Figure 6 Schematic depicting the experimental setup of Chevron Plate Heat Exchanger

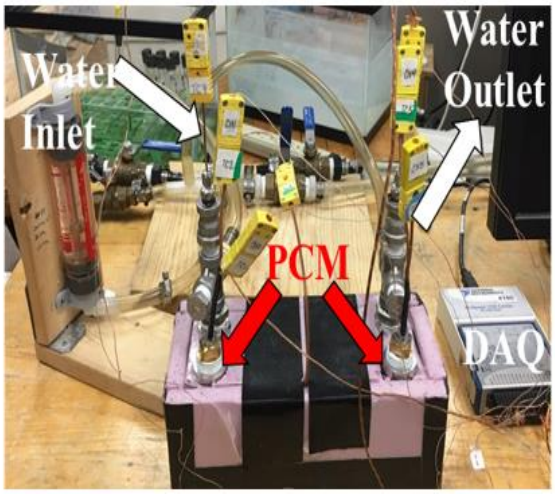

Figure 7 Image of the chevron plate heat exchanger experimental setup

The experimental setup consists of several components that enable the initiation of the melting or the solidification process and the control of volumetric flow rate of HTF. HTF is supplied to the Heat Exchanger from two constant temperature water baths (Cole-Parmer 12111-11). The hot/cold water from the water bath is supplied to the Heat Exchanger through a needle valve and flow meter (Omega FL-72 Series) arrangement in series. The vertical flowmeter has a measurement uncertainty of ±0.5 GPH.

The temperature of water at the inlet and outlet was measured using the wired "K"-type thermocouple (Omega, TT-K-24-SLE) with a measurement uncertainty of ±0.35°C. To measure the temperature of the PCM inside the Heat Exchanger, a total of 4 thermocouples (same type as mentioned above) were attached to the top and the bottom plates on both inlet and outlet side of the Heat Exchanger. All the water lines from the water bath to the Heat Exchanger were insulated to minimize the losses to the environment. The data was recorded using the NI 9211 DAQ Module with the NI 9213 Carrier. The Phase Change Material used is organic PureTemp® 29 and its properties are listed in table 7.

Since the heat exchanger suffers from a large metal to PCM ratio, the loss of energy through the metal was also estimated. The average heat capacity of the heat exchanger was estimated to be [0.323 kJ/(kg·K)] based on the data available in literature (Kumar 2018). The following table provides the specifications of the Chevron Plate Heat Exchanger used in this experiment.

Table 7 Specifications of the Heat Exchanger used in the study

Totals	Value	Unit
Total Empty Weight	1.222	kg
Mass of PCM	0.143	kg
Heat Transfer Area Per Plate	0.01155	m^2
Average Heat Capacity HX	0.323	kJ/kg. K
Metal to PCM Ratio	8.5: 1	

2.2.2 Experimental Procedure

The two isothermal water baths were maintained at 20°C and 38°C. Initially, water at 20°C from the cold water bath is supplied to the Heat Exchanger to initiate the solidification process. Once the steady state conditions were attained, the valve settings were adjusted to supply water from the hot bath to initiate the melting process. The system is allowed to reach steady state (temperatures of all thermocouples were within measurement uncertainty of ~ ±0.35°C) before the valves are switched back to continue to the next cycle. This procedure is repeated by varying volume flow rates and inlet temperature to the Heat Exchanger. Each test condition is repeated thrice to obtain the statistical uncertainty in the measured power and effectiveness. The test matrix for the experiment are tabulated below.

Table 8 Test Matrix for Chevron Plate Heat Exchanger Experiments

Flow Rate (GPH)	Temperature Range (°C)
5	T_{hot} = 38/34/32
	T_{cold} =20/24/26
8	T_{hot} = 38/34/32
	T_{cold} =20/24/26
10	T_{hot} = 38/34/32
	T_{cold} =20/24/26

2.2.3 Data Reduction and Uncertainty Analysis

The lack of an established method to evaluate the performance of a plate heat exchanger is a source of controversies caused by large variation in the results reported in literature by various authors. The energy storage analysis of a Chevron Plate Heat Exchanger was performed to determine the power rating of the heat exchanger by varying flow rates and inlet temperature of HTF. Estimation of the theoretical storage capacity of the PCM provides information on the heat losses in the system. Data reduction and uncertainty analysis discussed in *section 2.1.3* is also used for the Chevron Plate Heat Exchanger.

2.3 3D Printed Shell and Tube Heat Exchanger (12 point axial and radial PCM temperature mapping)

2.3.1 Experimental Setup

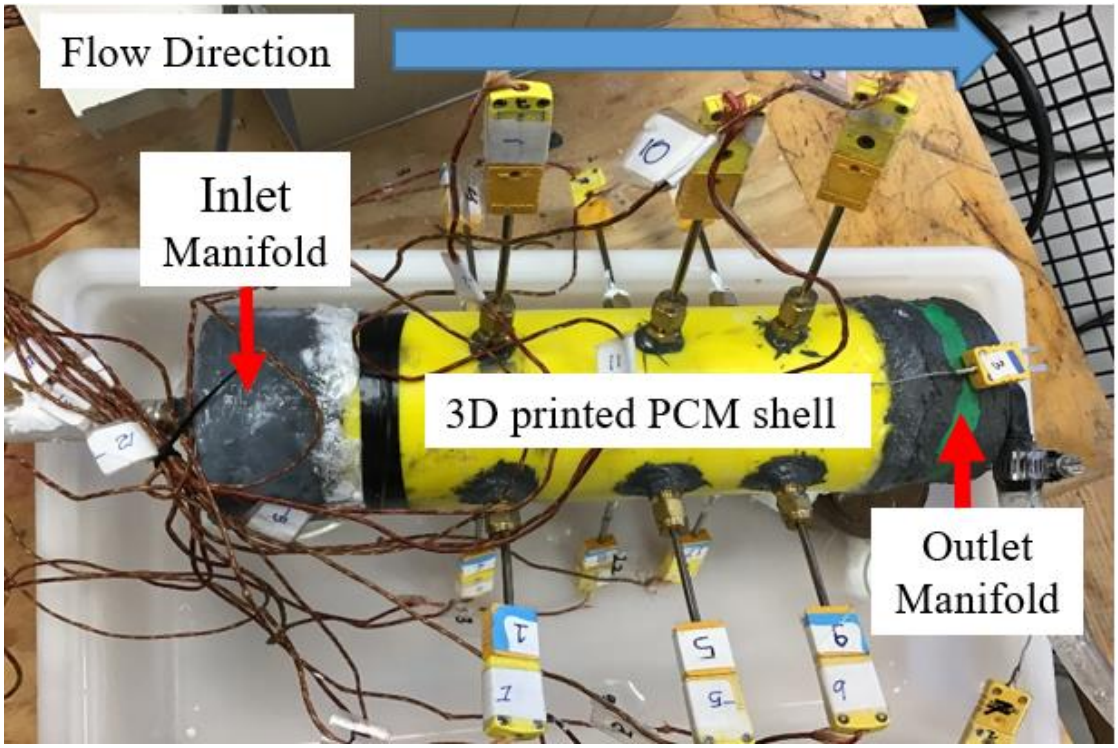

Figure 8 3D Printed Shell and Tube Heat Exchanger with thermocouples at varying axial and radial positions

A schematic and real time image of the experimental setup is shown in Figure 9 and 10 respectively.

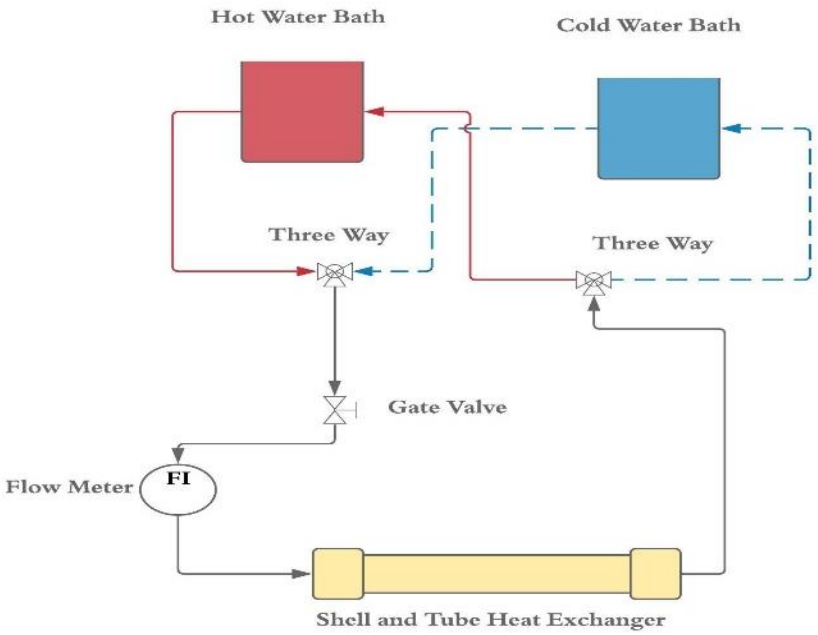

Figure 9 Schematic of the Flow Loop with the Heat Exchanger

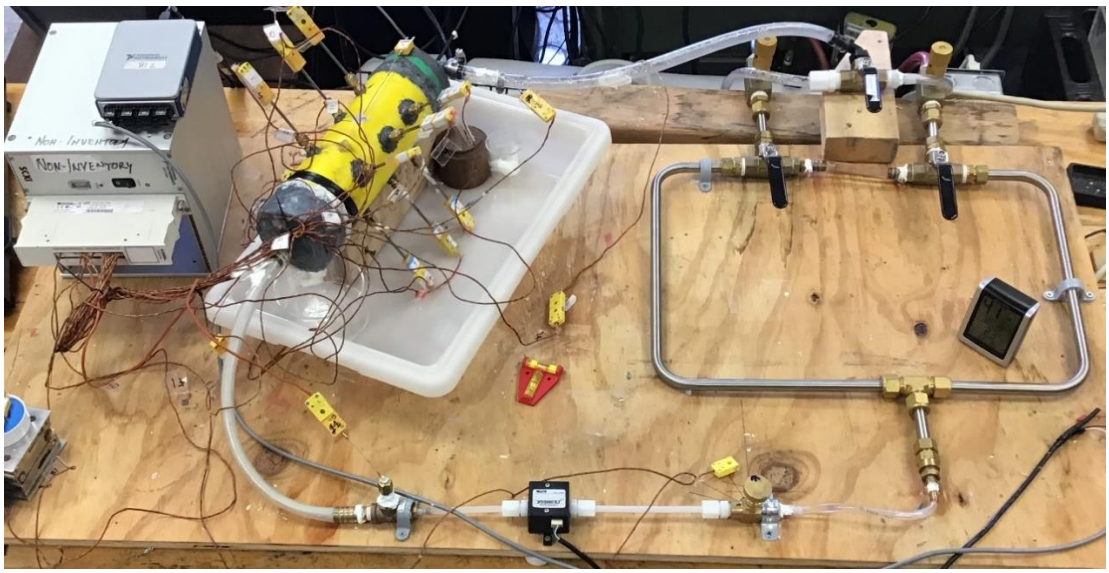

Figure 10 Real time image of the experimental apparatus. Collection beakers were placed at the bottom of the inlet manifold to capture the water/PCM leaks at the inlet manifold caused by porous 3D printed Shell

A total of 4 K-type shielded wire type thermocouples were used to measure the HTF temperature with a measurement uncertainty of ±0.8°C. The thermocouples were placed at the inlet and the outlet of the Heat Exchanger to measure the change in the temperature of the Heat Transfer Fluid (Water). To measure the temperature of the PCM and observe the propagation of the melt front, a total of 12 thermocouples were placed at varying radial and axial positions in the 3D printed shell. The position of the thermocouples in the shell is shown in the Table 9 and 3D schematic shown in Figure 11.

Table 9 Table showing the position of the thermocouples in the 3D printed shell. The angular positions are referenced to the axis of the heat exchanger whereas the vertical positions are referenced to the wooden block beneath the heat exchanger

Thermocouple Locations from Horizontal	**Inlet TCs**	**Mid TCs**	**Outlet TCs**	**Thermocouple Vertical Position**
45°	TC 1	TC 5	TC 9	Mid-Level-1 (Closer to Top)
135°	TC 2	TC 6	TC 10	Top
225°	TC 3	TC 7	TC 11	Mid-Level-2 (Closer to Bottom)
315°	TC 4	TC 8	TC 12	Bottom

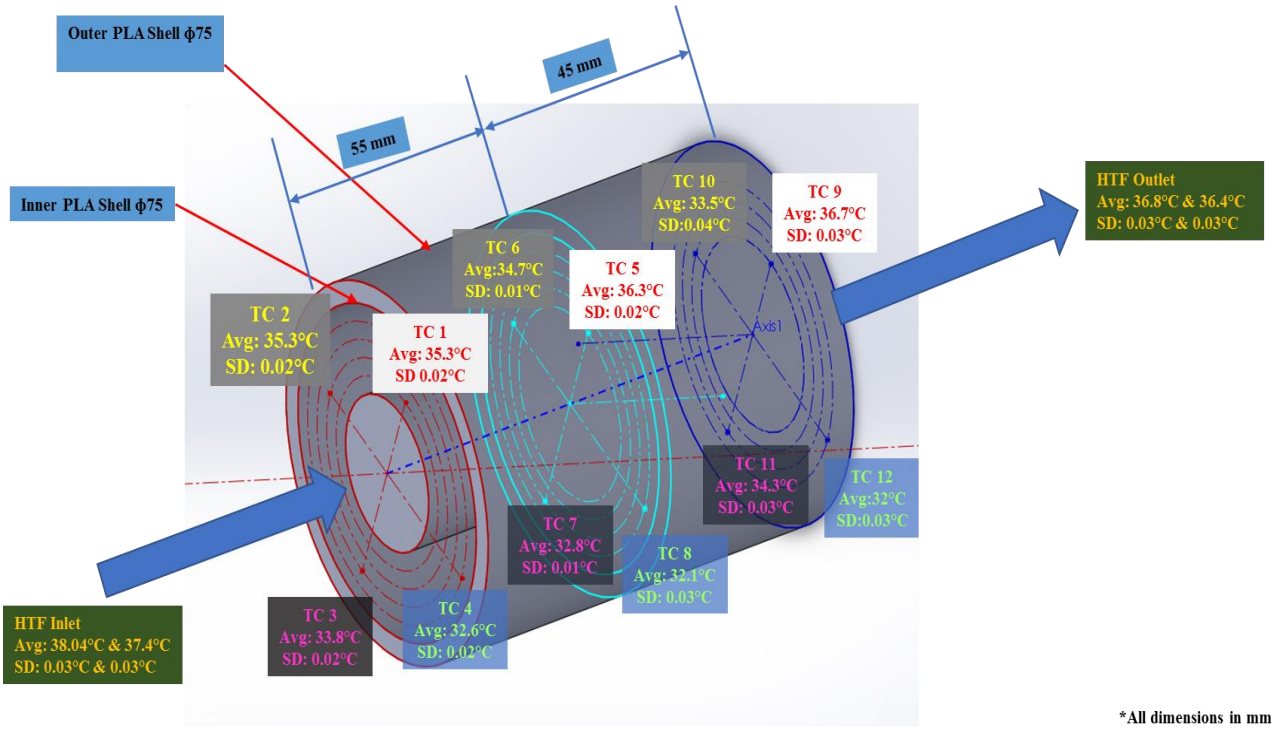

Figure 11 3D schematic depicting the radial and axial location of the thermocouples in the shell

The Phase Change Material used is organic PureTemp® 29 and its properties are given in Table 5. Based on the mass of the PCM loaded in the heat exchanger, the theoretical energy storage capacity of the Latent Heat Thermal Energy System (LHTESS) was estimated to be 94 KJ (464g in total with Storage Capacity of 202 J/g). The heat exchanger was placed horizontally on a wooden block and its level was verified using a spirit level. A slight tilt towards the inlet was observed due to the irregularities in the sealant application on the inlet and outlet HTF manifolds.

The thermocouples were calibrated in a water bath from 10°C to 40°C using a NIST calibrated thermometer (Least Count: 1°C and measurement uncertainty of ±0.5°C). The measurement uncertainty in the thermocouples was estimated to vary between ±0.8°C to ±1°C.

Temperature data was collected using the NI SCXI 1000 Chassis and NI SCXI-1303 board. Temperature was recorded at a sampling rate of 1 Hz frequency. To estimate the uncertainty in the thermocouple reading, the bias with the NIST thermometer, standard deviation of thermocouple readings, thermocouple sensitivity was estimated to be ±0.07°C were considered. Data acquisition error (ADC conversion) was neglected due to the low magnitude of this error (±0.003°C).

Omega FLR 1010 digital flowmeter was mounted at the inlet of the heat exchanger Flow Rate data was recorded by NI USB cDAQ 9161 with a frequency of 1 Hz. The flow meter was calibrated for a flow range of 0.2 L/min to 2 L/min as per the range specified by the manufacturer.

It should be noted that the thermocouples at the inlet needs to be calibrated after the experiment to correct the calibration constants as minor bends and strains might cause deviation from the original calibration. This is observed in all the 4 HTF thermocouples as the shielded wire type thermocouples can be strained easily.

Figure 12 Omega Flow Meter FLR 1010 used to measure the flow rate of HTF

Isothermal water baths used in the experiment were manufactured by Cole Parmer and VWR. The Cole Parmer Polystat was used as the hot bath and the VWR 1040 was use as the cold bath. Since both the isothermal baths had inbuilt pumps of varying capacities, the needle valve used in the experiment to control the flow was calibrated to obtain an approximately constant flow when switching between melting and solidification cycles.

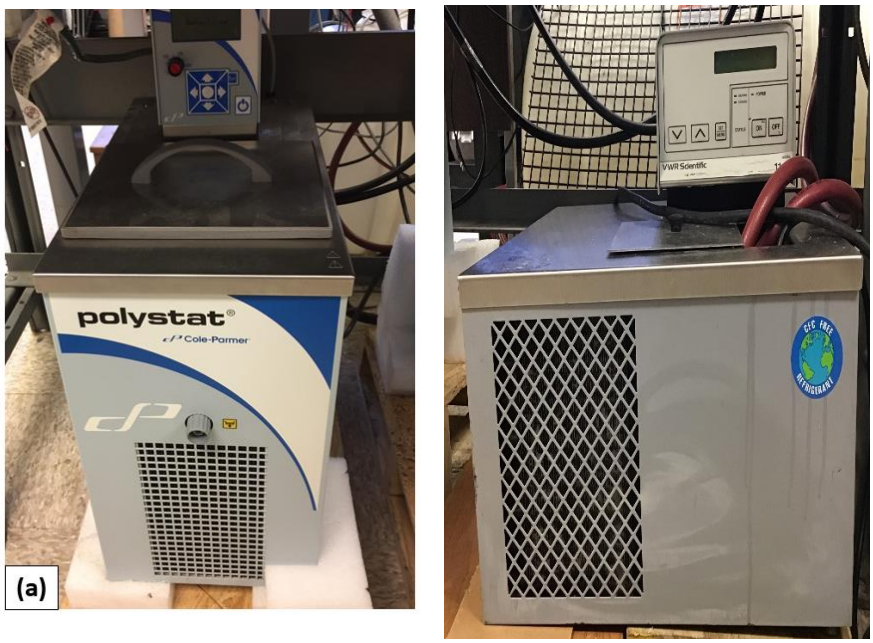

Figure 13 Water Baths. (A) Hot HTF, Cole-Parmer Polystat cooling/heating circulating bath (BOM# 212233800); (B) Cold HTF, VWR 1040 constant temperature controller

2.3.2 Experimental Procedure

The melting and solidification processes are initiated by supplying water from the isothermal hot and cold water baths respectively. Initially, the hot water bath is allowed to reach a steady state temperature of 38°C. Water from the hot bath is supplied to the heat exchanger to initiate the melting process. Once the PCM is completely melted, it is held for a sufficiently large time ~ 12 hours for the temperature readings to stabilize before supplying cold water from the cold bath to initiate the solidification process. The data is recorded for the solidification process at a given flow rate before the hot water is supplied to the heat exchanger to initiate the melting process. Every melt-freeze cycle is repeated twice to record the statistical uncertainty in the calculated parameters such as power and effectiveness. For this experiment, the inlet temperature of the hot and cold water is maintained at a constant temperature and the performance of the heat exchanger is analyzed for the melting and solidification process at varying flow rates as shown in the tables below.

Table 10 Melting Test Matrix for 3D Printed Shell and Tube Heat Exchanger (12 Point Axial and Radial Temperature Mapping)

Inlet Temperature of HTF (°C)	Flow Rate (GPH)
38	10
	7.5
	3

Table 11 Solidification Test Matrix for 3D Printed Shell and Tube Heat Exchanger (12 Point Axial and Radial Temperature Mapping)

Inlet Temperature of HTF (°C)	Flow Rate (GPH)
20	10
	7.5
	3

CHAPTER 3

RESULTS AND DISCUSSION

3.1 3D Printed Shell and Tube Heat Exchanger (single point PCM temperature measurement)

3.1.1 Melting Process

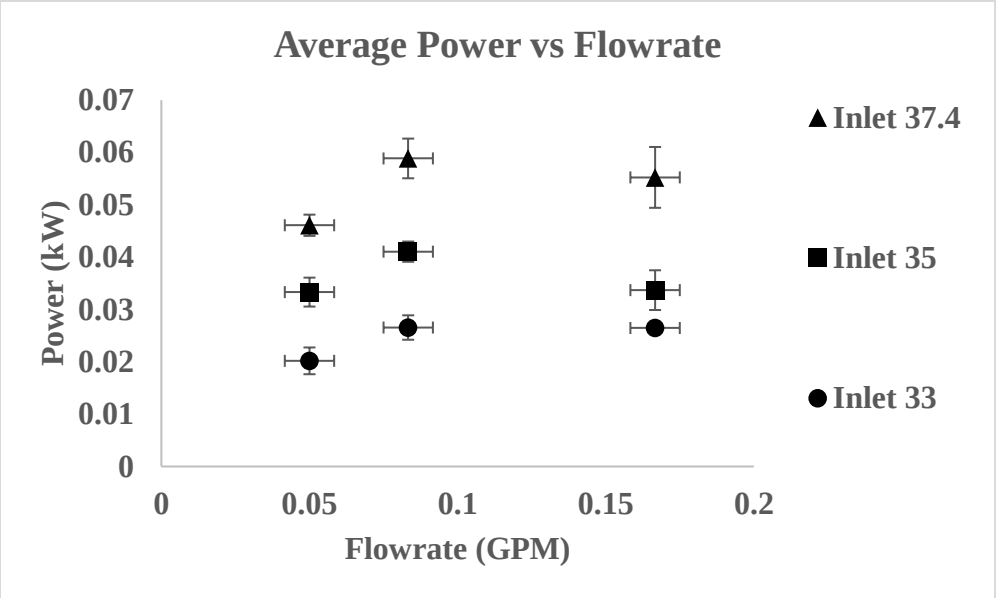

Figure 14 Average Power vs Flow Rate during melting for 3D printed shell and tube heat exchanger (single point temperature measurement)

From figure 14, it can be observed that the power is very sensitive to the inlet temperature of the HTF during melting. As the inlet temperature of the HTF is increased from 33°C to 37.4°C, it can be seen that the power increases by an average of ~100% for all the flow rates. The power rating also increases by ~48% and ~30% for inlet HTF temperature of 37.4°C and 33°C respectively as the flow rate is increased from 3GPH to 5 GPH. As the flow rate is further increased beyond 5 GPH, no significant change in the power ratings are observed in the experimental results. This

implies that there exists an optimal flow rate to attain maximum power rating of the heat exchanger where a balance between the loss to the ambient and rate of energy transfer can be realized.

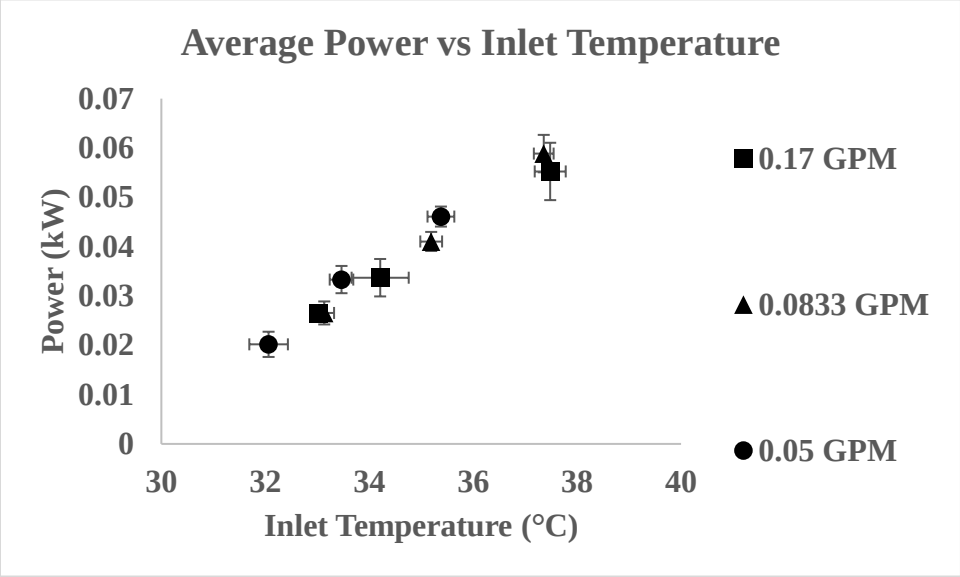

Figure 15 Average Power vs Inlet Temperature during melting for 3D printed shell and tube heat exchanger (single point temperature measurement)

However, the variation of power with the inlet temperature of heat transfer fluid (HTF) shows a steady increase with the increase in the inlet temperature of HTF at a given flow rate. This can be attributed to the fact that at elevated temperatures, the effect of natural convection within the shell of the heat exchanger enhances the power rating of the heat exchanger.

3.1.2 Solidification Process

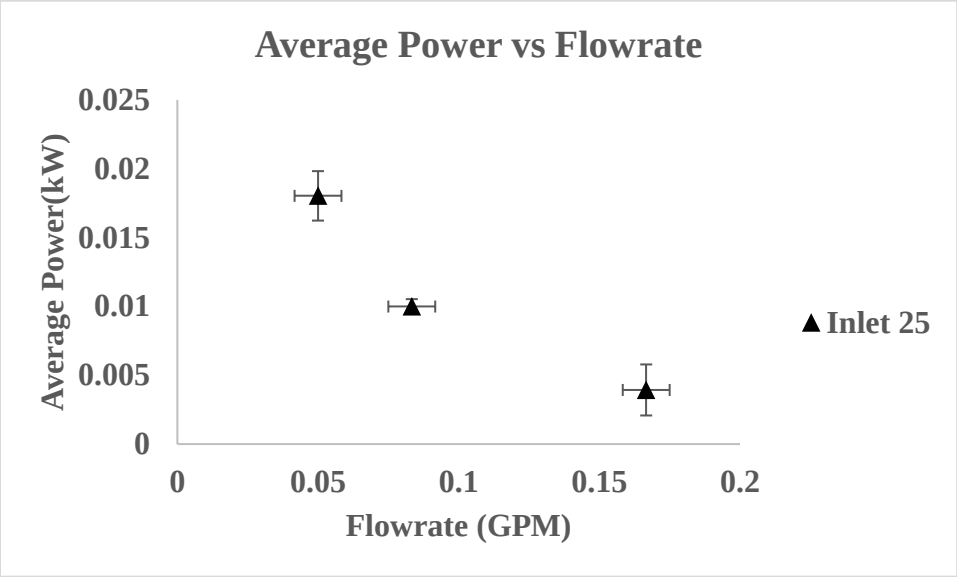

Figure 16 Average Power vs Flow Rate during solidification for 3D printed shell and tube heat exchanger (single point temperature measurement)

For solidification, the power value is maximum for 3 GPH and it reduces steadily through 10 GPH. This can be ascribed to the decreasing effective temperature difference of the heat transfer fluid (water) between the outlet and inlet as the flow rate is increased. Even though, the increasing flow rate is directly proportional to the power of the heat exchanger, the concurrent decrease in ΔT_{HTF} impacts the power rating at higher flow rates.

3.2 Chevron Plate Heat Exchanger

3.2.1 Melting Process

The Chevron Plate Heat Exchanger used in this experiment is a SWEP B5T with 0.01155 m^2 heat transfer area per plate. The plate heat exchanger is filled with liquid PCM on the LHSU side. As mentioned earlier, this experiment was performed with organic PureTemp 29® as PCM. The selected PCM has a theoretical phase transition temperature of 29°C. Thus, the temperature of the hot water bath was varied between 32°C to 38°C. The temperature of the cold water bath was varied between 20°C to 26°C. The flowrates tested in the experiment are 5 GPH, 8 GPH and 10 GPH respectively. Each combination of hot water temperature, cold water temperature and flow rate were repeated three times to record the statistical uncertainty for the measured parameters.

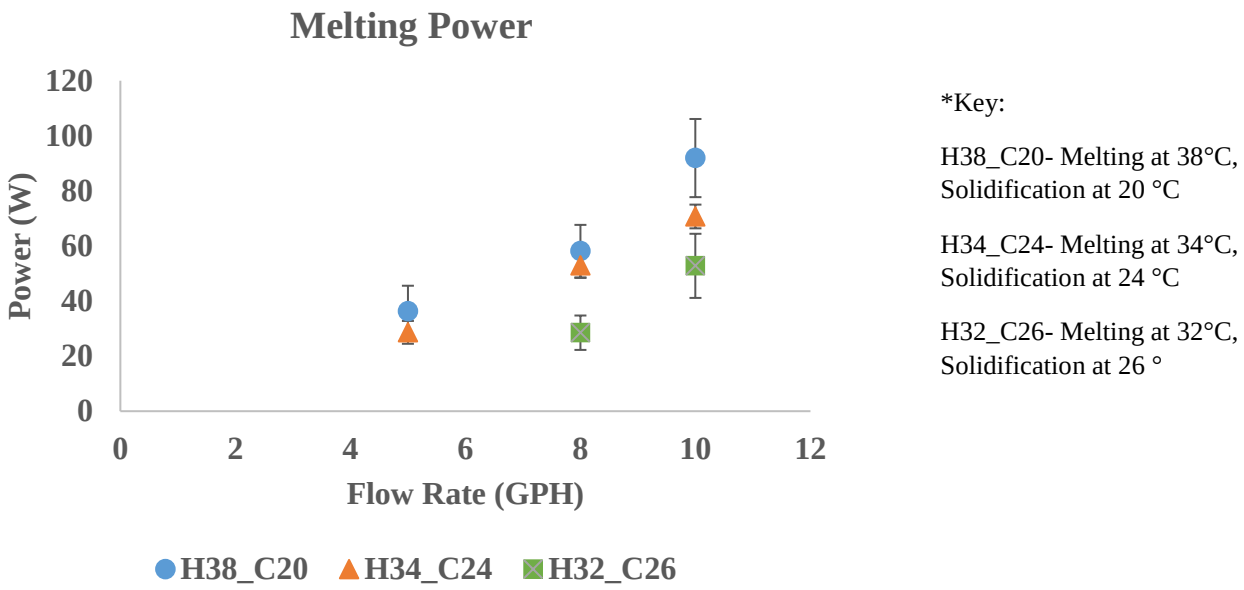

Figure 17 Average power vs flow rate during melting for chevron plate heat exchanger

As depicted in Figure 17, power is a function of both flowrate and inlet temperature of heat transfer fluid (HTF). As the inlet temperature of heat transfer fluid (HTF) is increased, the power value increases for a given flow rate. The increment is more pronounced at higher flow rates with an increment of about 70% at 10 GPH compared to 28% at 5GPH. For a constant inlet temperature of heat transfer fluid (HTF), the power value increases more rapidly with an average increment of about 100% as the flow rate increases from 5 GPH to 10 GPH. This effect again, is more pronounced at the highest inlet temperature with an enhancement of 1.5 times the original value at 5 GPH.

This is anticipated as the power rating of the heat exchanger is dependent on the time duration of the melting or solidification process. Since the time duration of the melting process is effectively decreased as the flow rate increases, power increases with the flow rate. Additionally, the power rating is also found to be more sensitive to the flow rate when compared to the inlet temperature of the heat exchanger.

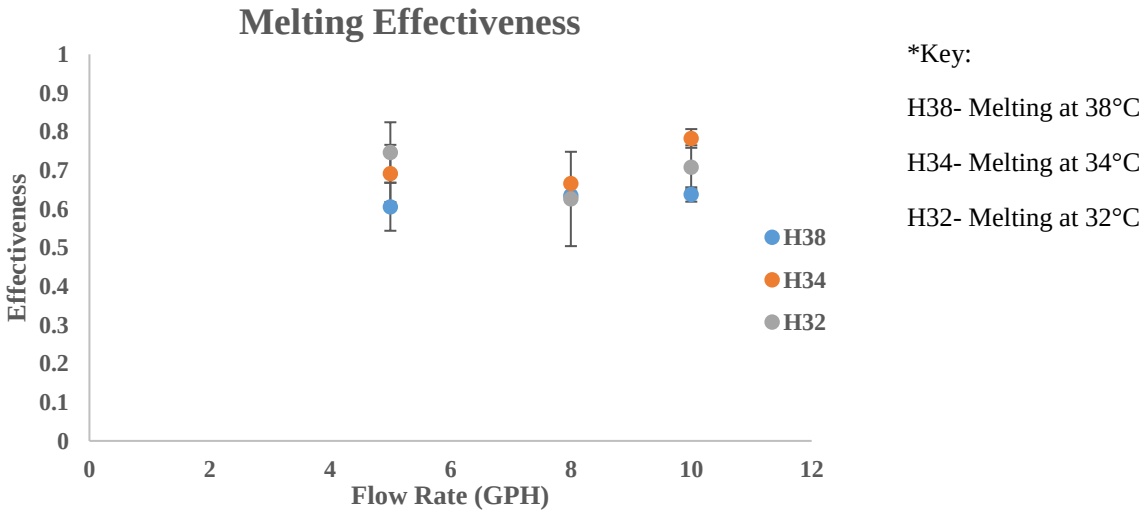

Figure 18 Average Effectiveness vs Flow Rate during melting for chevron plate heat exchanger

Effectiveness for the melting process is plotted in Figure 18. From the graph, it can be observed that the effectiveness is marginally higher at higher flow rates. However, the variation in the experimental time for the melting process is large and hence the statistical uncertainty of the calculated effectiveness is also high. Thus, it can be assumed that the value of effectiveness remains virtually constant as the flow rate is increased. Additionally, the effect of natural convection in reducing the melt time and hence improving the power rating is not pronounced in the plate heat exchanger. This can be attributed to the limited volume between the plates for the PCM to convect naturally and enhance the rate of heat transfer.

3.2.2 Solidification Process

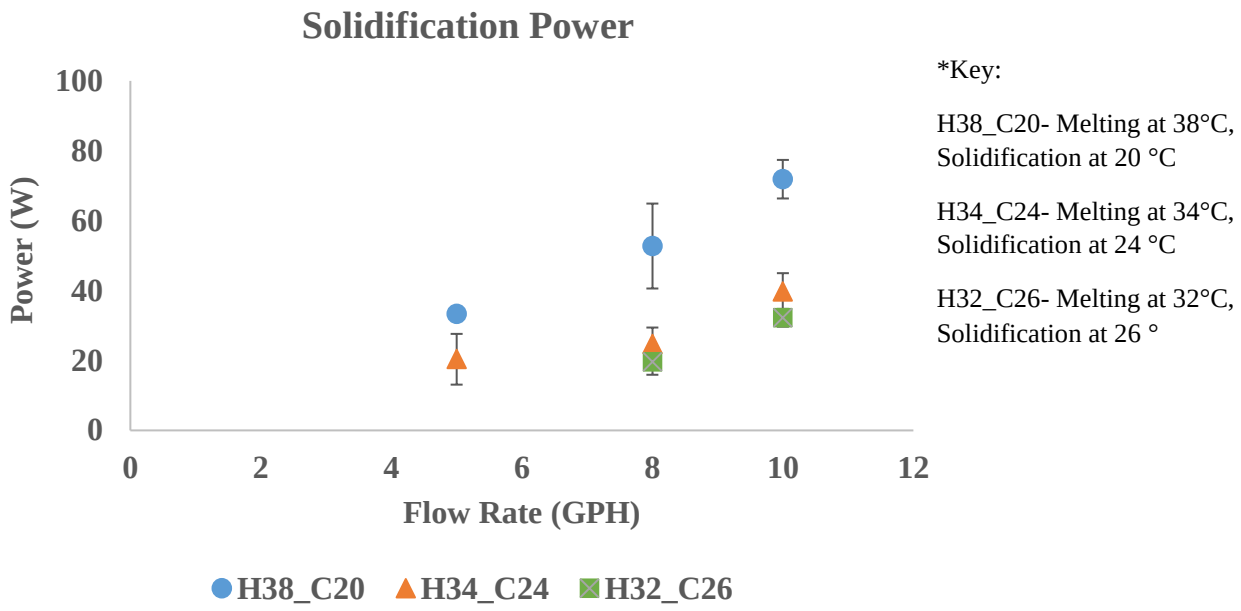

Figure 19 Average power vs flow rate during solidification for chevron plate heat exchanger

For solidification, power is again a function of both flow rate and inlet temperature of the heat transfer fluid (HTF). In general, the power value is consistently lower than that obtained during charging for the same inlet temperature of HTF and flow rate. For constant inlet temperature of the heat transfer fluid (HTF), the power increases as the flow rate is varied from 5 GPH to 10 GPH. An average increment of 115% is observed for the aforementioned condition. Similarly, an increment of 70% is observed by varying the inlet temperature of the heat transfer fluid (HTF) keeping the flow rate constant.

In general, for both melting and solidification, an increase in the power rating is observed for both increasing flow rate and increasing inlet temperature of heat transfer fluid (HTF) is observed. The effectiveness for both the melting and solidification processes are identical with the higher

variation at the lowest 5 GPH flow rate. However, the variation is within the bounds of measurement uncertainty and hence, the overall effectiveness of the Chevron Plate Heat Exchanger with PCM can be assumed to be constant with the variation in the flow rate and cold inlet temperature of the cold fluid (HTF).

The range of effectiveness for the solidification process is observed to be between ~0.6 and 0.8. With this observation, it is evident that the performance of the metal plate heat exchanger is governed by the parasitic losses to the ambient as the solidification effectiveness should theoretically be higher for a constant inlet temperature of the HTF at lower flow rates due to higher values of $(\Delta T)_{HTF}$ (between inlet and outlet).

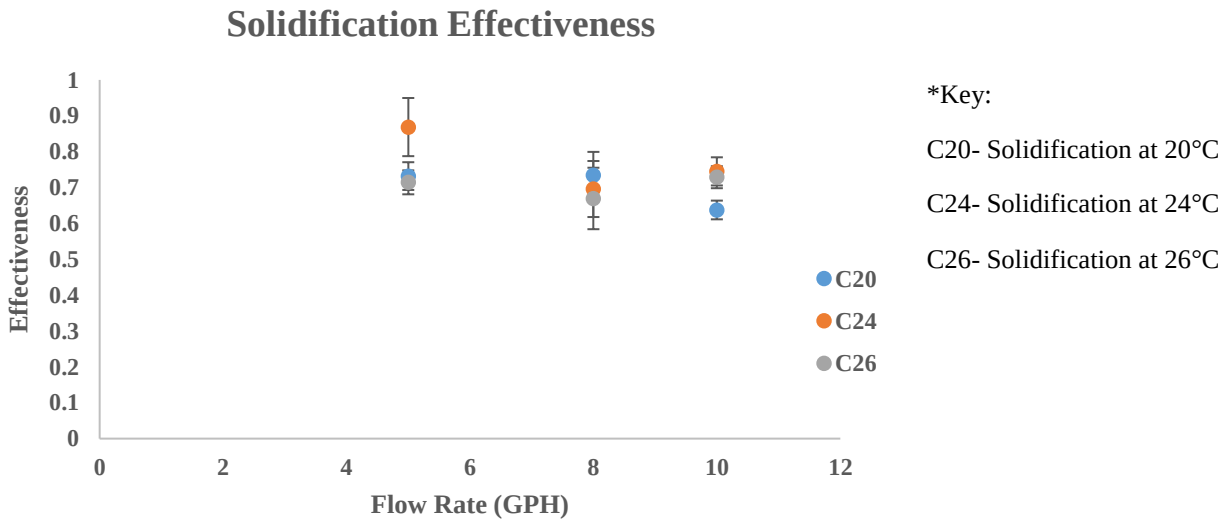

Figure 20 Average Effectiveness vs Flow Rate during solidification for chevron plate heat exchanger

3.3 3D Printed Shell and Tube Heat Exchanger (12 point axial and radial PCM temperature mapping)

3.3.1 Melting Process

3.3.1.1 ***Axial Melt Front Propagation***

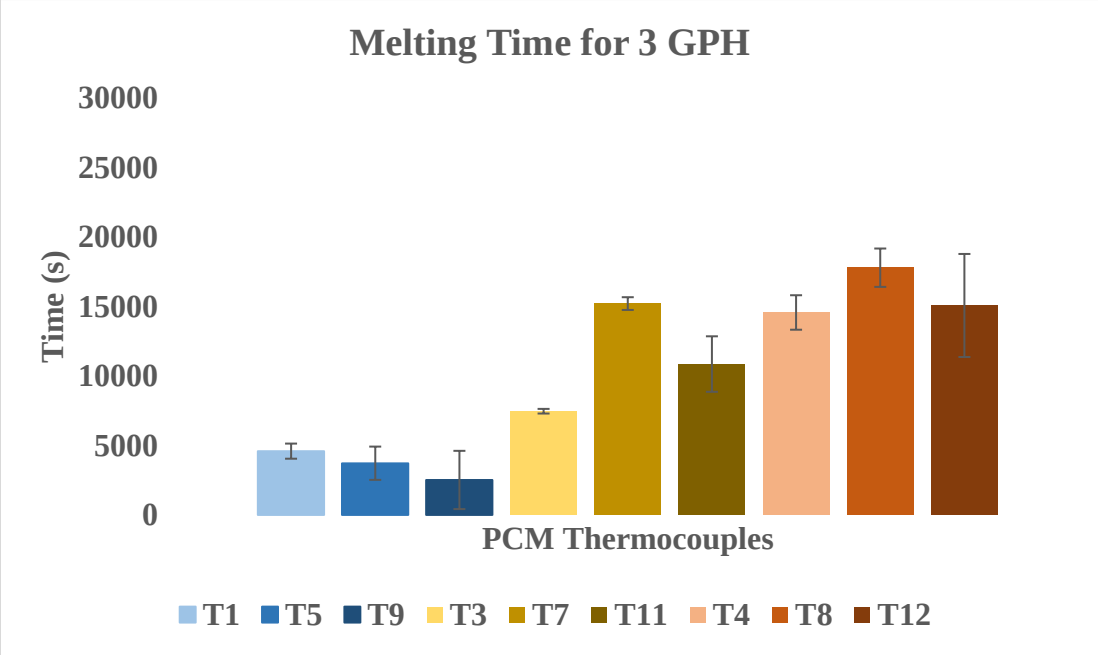

Figure 21 Variation of phase transition time for 3 GPH at varying axial and radial locations during melting for 3D printed shell and tube heat exchanger (12 point temperature measurement)

Figure 21 shows the phase transition time for the thermocouples at varying axial and radial positions in the PCM for the shell of the Heat Exchanger. The thermocouples are grouped and color coded based on their axial and radial locations. For instance, T1, T5 and T9 (blue series) are at the same radial position with T1 closer to the inlet (section 1), T5 at the mid-section (section 2) and T9 closer to the outlet (section 3). The inlet section and mid-section are 45 mm apart whereas the outlet section and the inlet section are 100 mm apart. The blue series thermocouples are located

at the same radial distance of 16 mm from the inner wall of the shell. Similarly, the yellow series and the brown series of thermocouples are located at a radial distance of 8 mm and 4 mm from the outer wall of the PCM tube respectively. In simple terms, the blue series denotes the innermost thermocouples and the brown series denotes the outermost thermocouples in the PCM shell. The variation of the axial distance within the same series of thermocouples is represented by a variation in the shade of the series color. For instance, in the blue series, T1 has the lightest shade of blue and represents section closest to inlet. Similarly, T9 has the darkest shade of blue and thus represents the section closest to the outlet. All the mid-section thermocouples are represented by a shade intermediate to the lightest and darkest shade of the corresponding series color.

For the blue series, it can be seen that the melting phase transition time is in the same range at all the axial locations. However, a clear pattern is evident in both the yellow and brown series. From Figure 21, it can be seen that the PCM at the mid-section (section 2) takes longer duration to transition from the solid phase to the liquid phase. However, PCM at section 3 shows a longer phase transition than at section 1. This is understandable as the section 1 is exposed to the highest temperature of HTF. As the axial distance increases, the transfer of thermal energy from the HTF to PCM causes the temperature of the HTF to drop in the axial direction. This also explains the longer phase transition time for PCM at section 2 when compared to section 1. However, the PCM at section 2 has a longer phase transition time than the PCM at section 3 because of the heat conduction form progressive water accumulation at the outlet segment of the HTF manifold. This helps to reduce the phase transition time of the PCM at the section 3 considerably when compared to the PCM at section 2. It should also be noted that the head of water built up within the outlet manifold is higher than the position of thermocouples in the yellow and brown series. This explains

the reason for a more uniform axial melt front propagation in the blue series in addition to the effect of thermal energy transfer from the HTF.

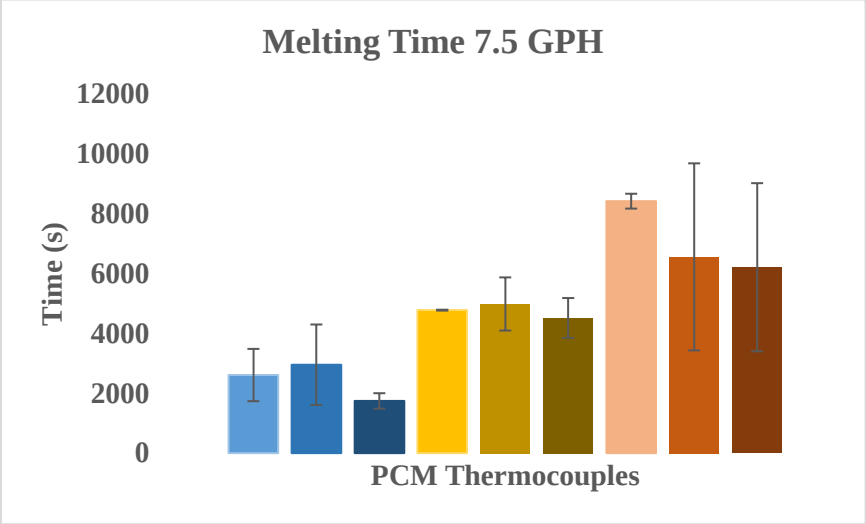

Figure 22 Variation of phase transition time for 7.5 GPH at varying axial and radial locations during melting for 3D printed shell and tube heat exchanger (12 point temperature measurement)

The axial melt front propagation for 7.5 GPH shows a similar pattern. From figure 22, it can be seen that the variation of phase transition times at the same radial location along the axis is predominantly smaller possibly because of the higher volumetric flow rate of HTF. Also, the average phase transition time for the blue series is reduced by 32% in comparison to the 3 GPH case. For the yellow series and the brown series, the phase transition times are reduced by ~55% in comparison to the 3 GPH trials.

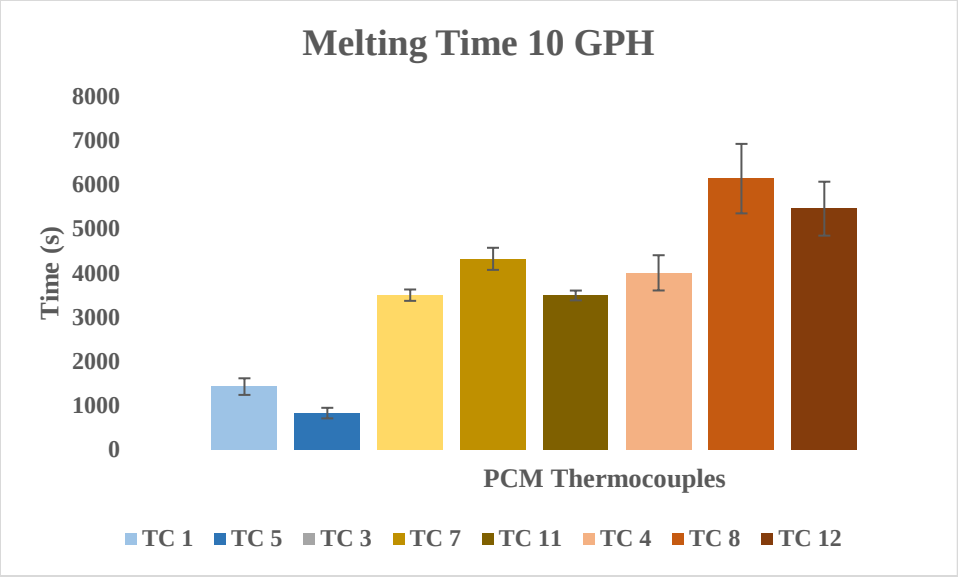

Figure 23 Variation of phase transition time for 10 GPH at varying axial and radial locations during melting for 3D printed shell and tube heat exchanger (12 point temperature measurement)

For 10 GPH, the average phase transition time is further reduced due to increased volumetric flow rate. The phase transition times are reduced for the blue, yellow and brown series are reduced by ~ 79%, 66% and 67% respectively in comparison to that of the 3GPH case.Figure 1

3.3.1.2 Radial Melt Front Propagation

In general, it can be observed that the phase transition time for the blue series is the lowest. This is anticipated as the blue series thermocouples are the closest to the hot HTF stream flowing in the steel tubes. As the radial distance from the center of the shell increases, the phase transition time also increases. This is understandable as the melt front propagates radially outward initially. Also, it is noteworthy to mention that each series of thermocouples are at different vertical heights from the reference wooden block on which the heat exchanger is mounted. This is specifically important at later stages of the melting process as it impacts the melt front propagation. The variation in the density of the melt and solid PCM causes an onset of natural convection within the PCM shell. Hence, the thermocouples at the bottom of the PCM shell (brown series) have the longest duration of phase transition as shown in figure 24.

Hence, it can be concluded the experimental phase transition times observed in the experiment are a result of the combined effect of the outward propagation of melt front and density gradients within the PCM shell during the melting process.

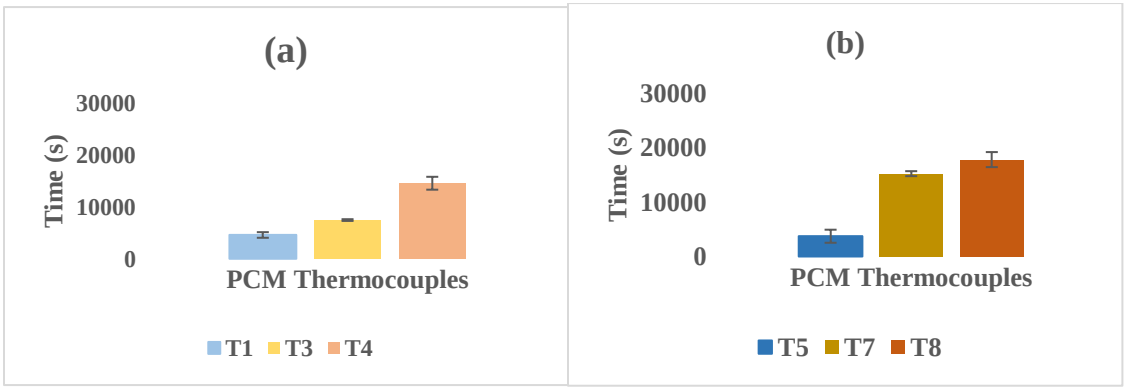

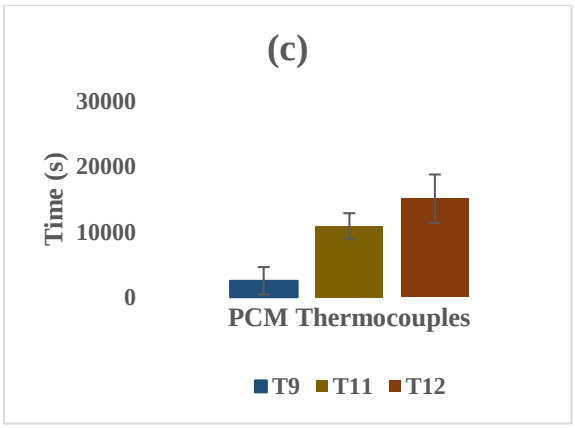

Figure 24 Variation of phase transition time for 3GPH during melting at varying radial locations for 3D printed shell and tube heat exchanger (12 point temperature measurement) (a) Section 1 (b) Section 2 (c) Section 3

At higher flow rates, the same trend for radial melt propagation trend was observed. However, the phase transition times are roughly shortened by 50% for 7.5 GPH and 70% for 10 GPH in comparison to that of the 3 GPH cases. The variation of phase transition time at the different radial locations for section 1, section 2 and section 3 are shown in the figure 25 and figure 26.

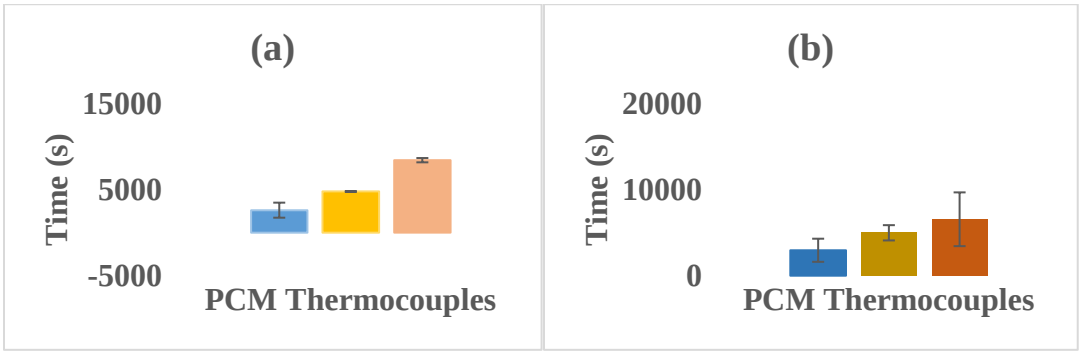

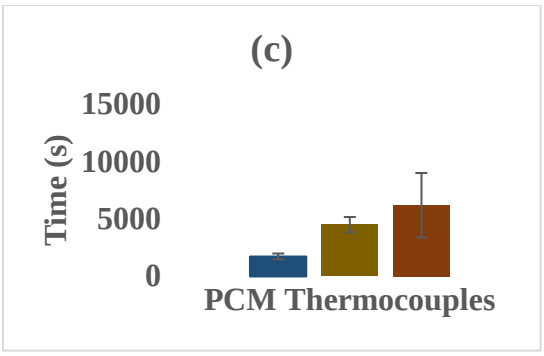

Figure 25 Variation of phase transition time for 7.5 GPH during melting at varying radial locations for 3D printed shell and tube heat exchanger (12 point temperature measurement) (a) Section 1 (b) Section 2 (c) Section 3

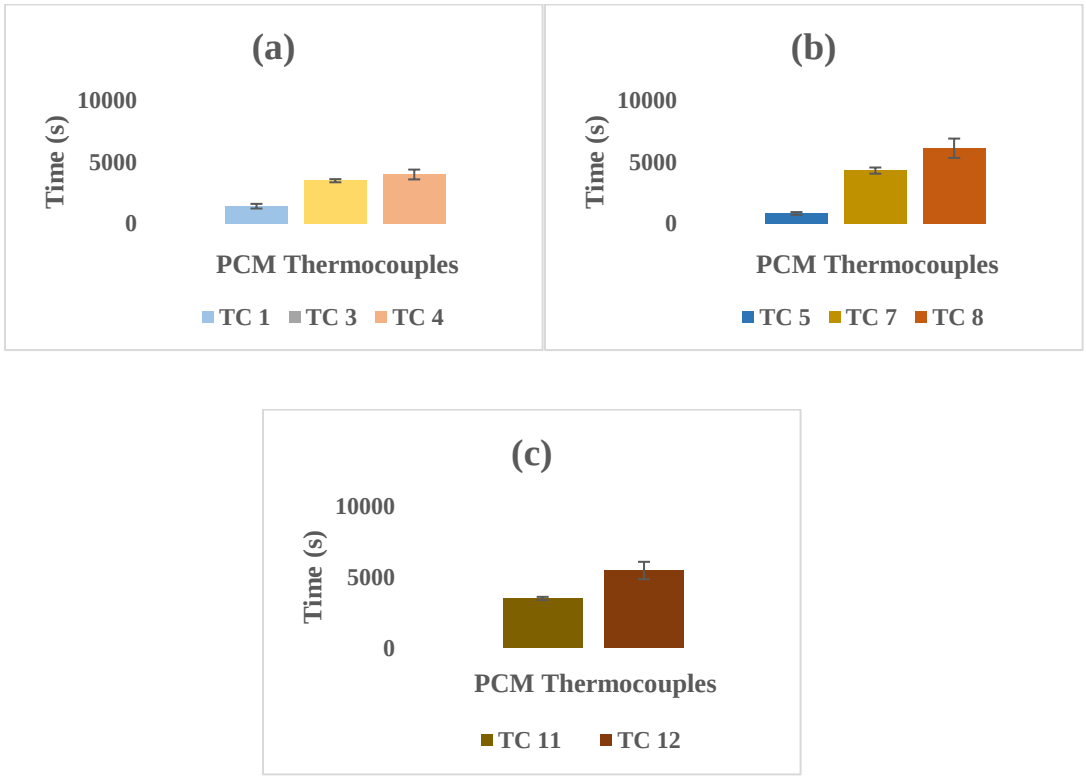

Figure 26 Variation of phase transition time for 10 GPH during melting at varying radial locations for 3D printed shell and tube heat exchanger (12 point temperature measurement) (a) Section 1 (b) Section 2 (c) Section 3

3.3.2 Solidification Process

3.3.2.1 Axial Freeze Front Propagation

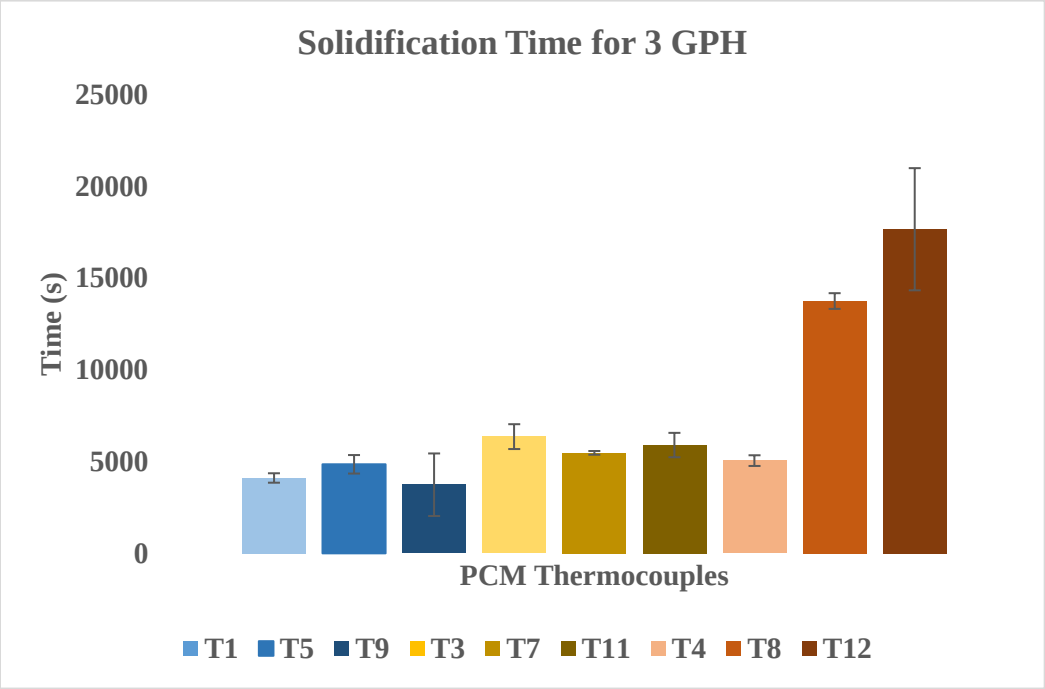

Figure 27 Variation of phase transition time for 3 GPH at varying axial and radial locations during solidification for 3D printed shell and tube heat exchanger (12 point temperature measurement)

From figure 27 it can be observed that the freeze front propagation is approximately uniform at several locations and shows lower variability than the melting cases. This is expected as energy transfer during solidification is dominated by conduction only. Thus, it is expected that the PCM closest to the inlet will complete phase transition before the other regions. This trend can be observed in Figure 26. The axial variation is evident in the brown series and not clearly visible in the other series as both the blue and yellow series thermocouples are surrounded by stainless steel tubes carrying cold HTF. Since the freeze front propagates radially outward in the cylindrical shell

and the average HTF temperature gain (ΔT) during solidification is lower than that of the melting cases, the lower magnitude of variations in the phase transition times along the axis for the blue and yellow series can be justified. However, an axial propagation of freeze front is clearly seen in the brown series as the thermocouples belonging to this series are not embedded in the array of HTF carrying tubes. Thus, PCM at section 3 takes the longest time for phase change.

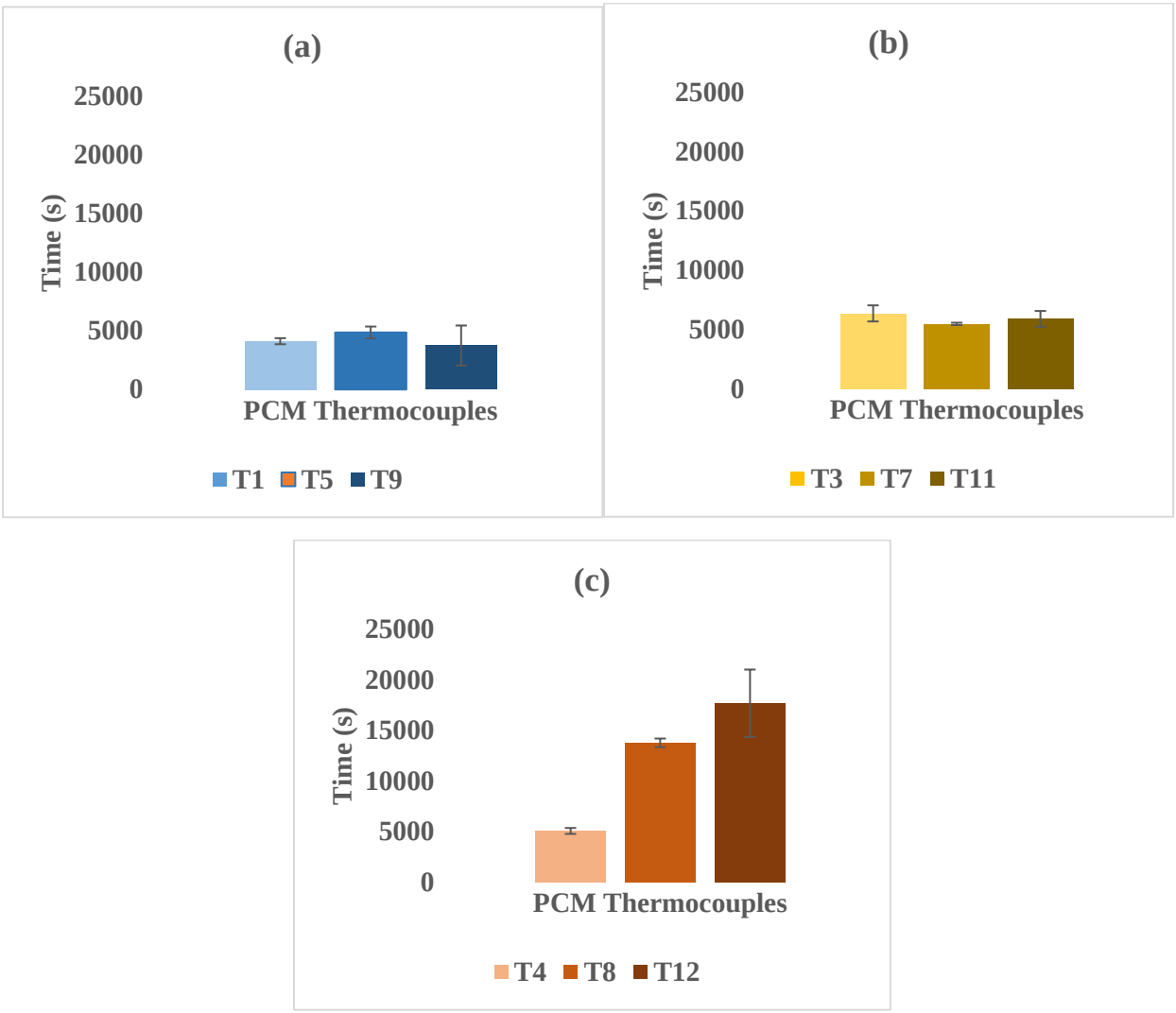

Figure 28 Variation of phase transition time for 3GPH during solidification for 3D printed shell and tube heat exchanger (12 point temperature measurement) at varying axial locations (a) Innermost radially (b) Radial middle (c) Outermost radially

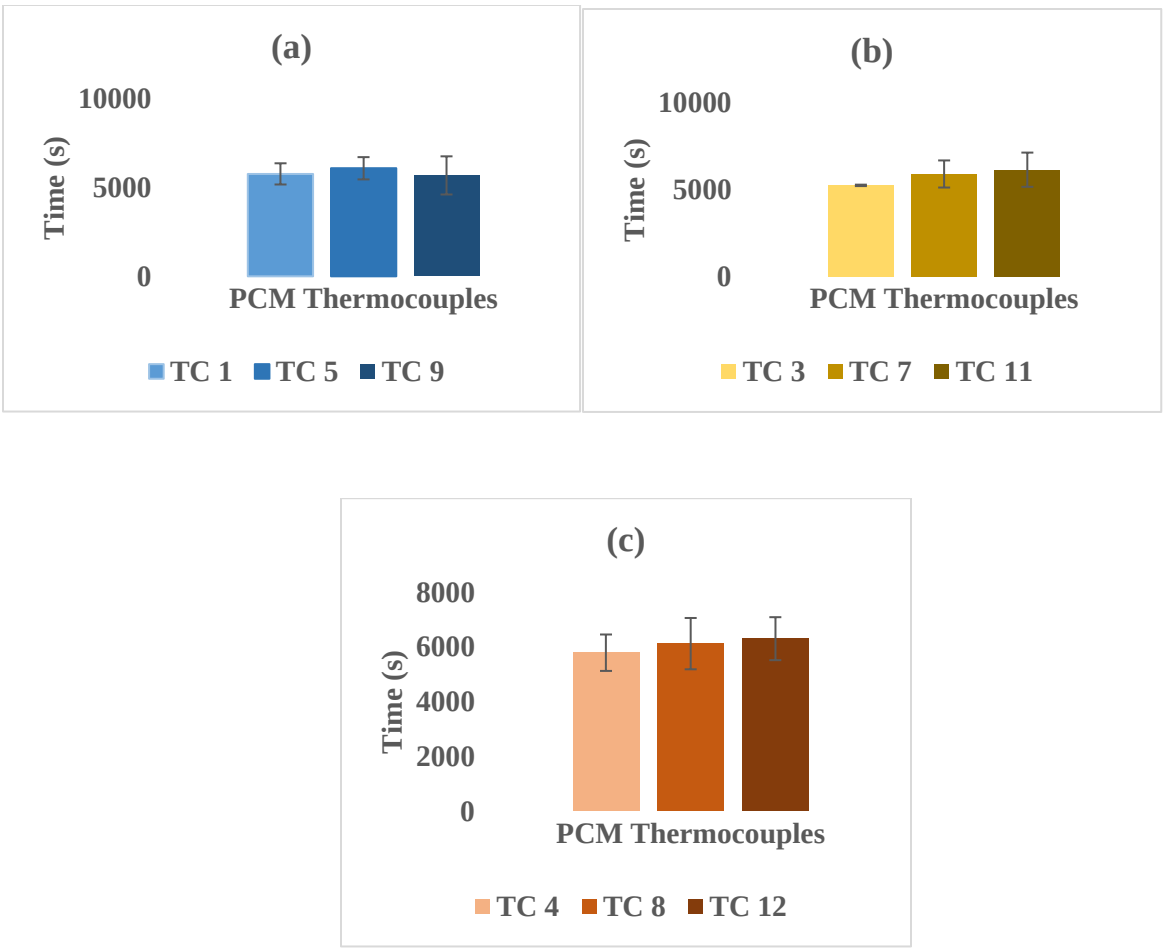

Figure 29 Variation of phase transition time for 7.5 GPH during solidification for 3D printed shell and tube heat exchanger (12 point temperature measurement) at varying axial locations (a) Innermost radially (b) Radial middle (c) Outermost radially

From Figure 29, it can be seen that the axial propagation of the freeze front for 7.5 GPH cases are similar to that of the 3 GPH cases. However, the phase transition times are reduced by ~ 55% and 65 % for the PCM in the vicinity of the thermocouples TC 8 and TC 12, since higher flow rates of HTF causes higher energy transfer rate. However, none of the other regions show a significant variation in the phase transition time in comparison to that of the 3 GPH cases as the thermocouples in the other regions are embedded in the array of the HTF tubes.

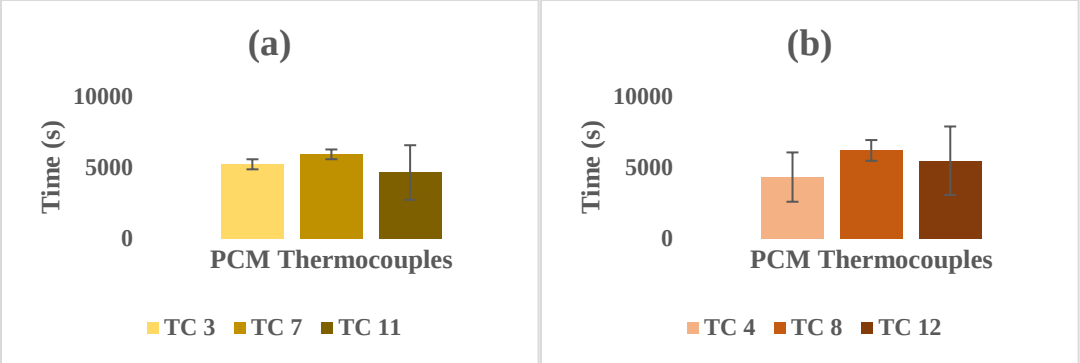

Figure 30 Variation of phase transition time for 10 GPH during solidification for 3D printed shell and tube heat exchanger (12 point temperature measurement) at varying axial locations (a) Radial middle (b) Outermost radially

For 10 GPH, the axial propagation of the freeze front is similar to that at 3GPH and 7.5 GPH for the yellow series. However, the phase transition time for the PCM in the vicinity of the thermocouples TC 8 and TC 12 are reduced by ~55% and 70% respectively.

3.3.2.2 Radial Freeze Front Propagation

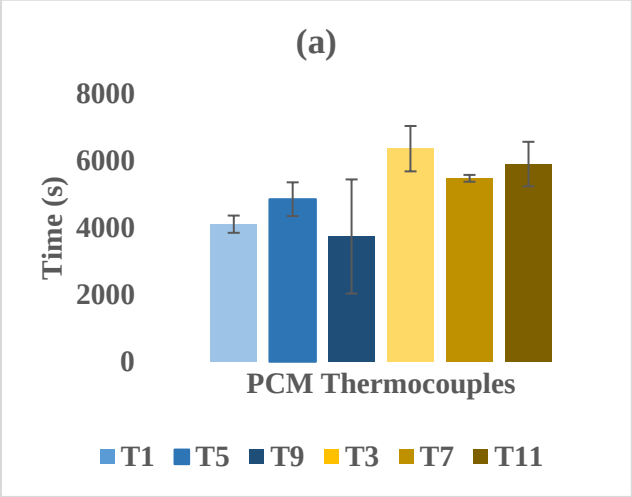

Figure 31 Variation of phase transition times at 3 GPH during solidification for blue and yellow series

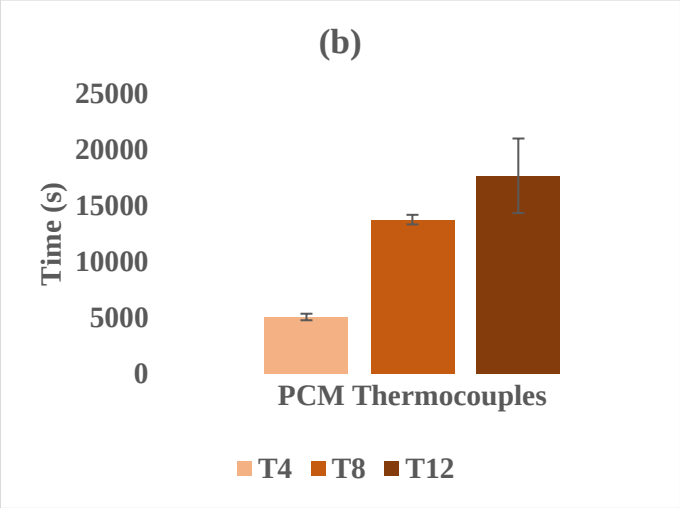

Figure 32 Variation of phase transition times at 3 GPH during solidification for brown series

From Figure 31, it can be observed that there is very little axial variation in the phase transition times for both the blue and yellow series. However, a slight increase in the average phase transition

time for the yellow series is observed in comparison to the blue series due to the propagation of the freeze front radially outward. The brown series takes the longest to complete the phase transition as it is far from the center of the shell. An axial time variation is also observed in the brown series which is explained in section 3.3.2.1.

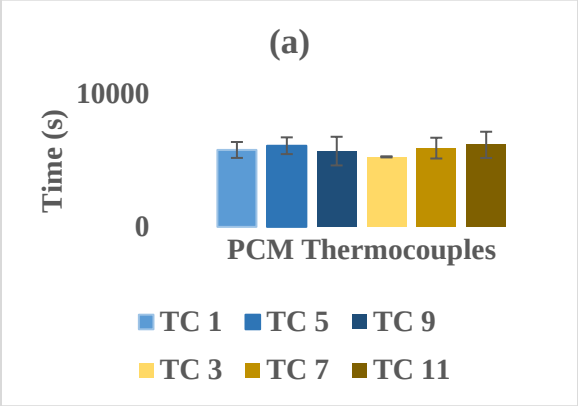

Figure 33 Variation of phase transition times during solidification for blue and yellow series at 7.5 GPH

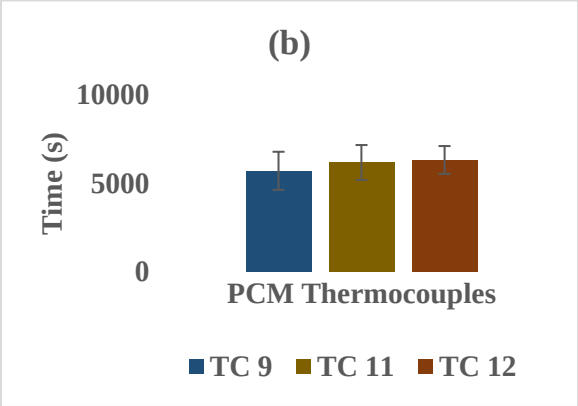

Figure 34 Variation of phase transition times during solidification for 7.5 GPH at section 3 thermocouples

In comparison to the 3GPH cases, the general trend of radial freeze front propagation is not clearly noticeable at 7.5 GPH. This could be caused by the higher energy transfer rate into the HTF in

comparison to that of the 3 GPH case. Thus, a more uniform radial and axial melt propagation is seen at 7.5 GPH.

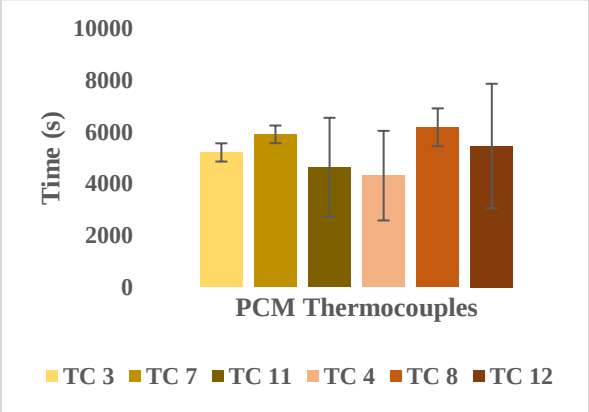

Figure 35 Variation of phase transition times during solidification for yellow and brown series at 10 GPH

Similarly, for 10 GPH, a uniform distribution of the phase transition time could be observed for the yellow and brown series similar to that of the 3 GPH and 7.5 GPH cases.

3.3.3 Power Calculations

3.3.3.1 Melting Process

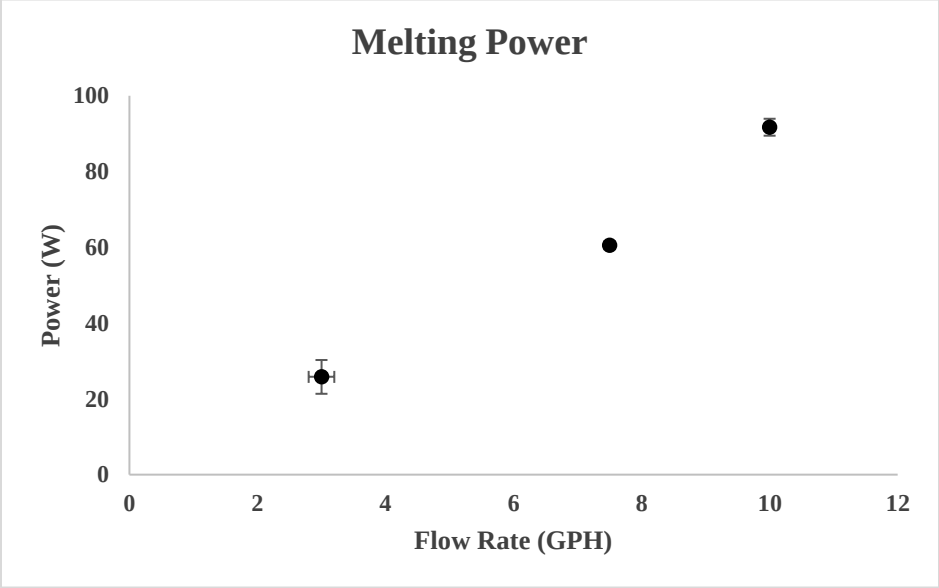

Figure 36 Melting Power for 3D printed shell and tube heat exchanger (12 point temperature measurement) at an inlet temperature of 38°C

From the Figure 36 it can be seen that the power rating of the heat exchanger for the melting cycles increases as the flow rate increases. As discussed in the sections 3.1 and 3.2, the melting power increases at higher flow rates due to the decrease in the phase transition time caused by faster energy transfer rate. By performing a simple energy balance at a small section of the HTF tubes, it can be shown that the rate of transfer of heat from the hot HTF is dependent on the mass flow rate. An enhancement of ~ 1.3 and ~2.5 times the power rating at 3 GPH is observed at 7.5 GPH and 10 GPH for the same inlet temperature of HTF at 38°C.

3.3.3.2 Solidification Process

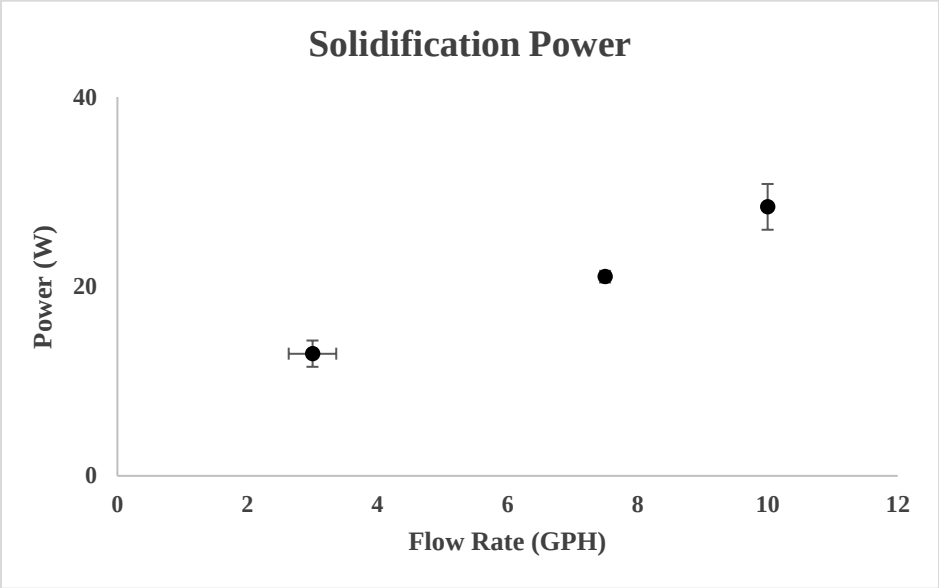

Figure 37 Solidification Power for 3D printed shell and tube heat exchanger (12 point temperature measurement) at an inlet temperature of 20°C

From Figure 37, it can be observed that the average power for the solidification also increases as the flow rate is increased. However, the enhancement in the average power with flow rate is lower during solidification. The higher average power observed during the melting process could be attributed to the effect of natural convection that enhances the heat transfer between the HTF and the PCM.

3.3.4 Effectiveness Calculations

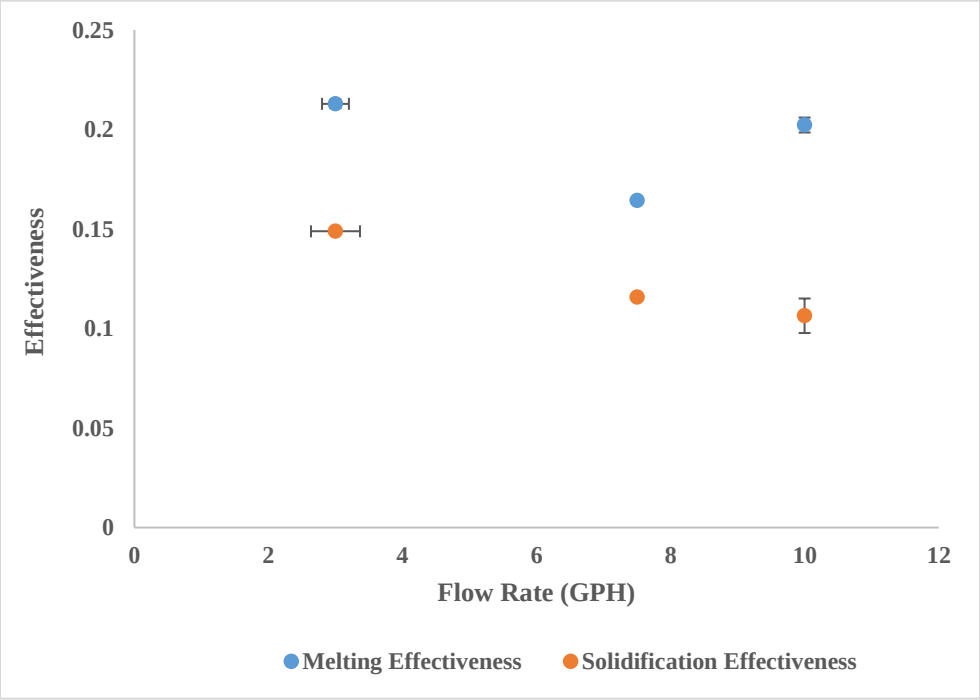

Figure 38 Effectiveness for 3D printed shell and tube heat exchanger (12 point temperature measurement)

The effectiveness for the heat exchanger is found to increase as the flow rate is decreased from 10 GPH to 3 GPH during solidification. This could be caused by the higher average ΔT_{HTF} observed at lower flow rates. This higher ΔT_{HTF} at lower flow rates could be caused by a greater residence time of the HTF in the heat exchanger at lower flow rates. Hence, the higher heat exchanger effectiveness at lower flowrates for solidification can be justified. Additionally, the effectiveness is consistently higher at all the flow rates for melting process. For all flow rates, an average enhancement of ~50% is observed for the melting process when compared to its corresponding solidification value.

CHAPTER 4

CONCLUSION AND RECOMMENDATIONS

4.1 Summary of Results

In this study, the thermal performance characteristics of two heat exchangers were explored: (a) a 3D Printed Shell and Tube heat exchanger; and (b) a commercial chevron plate heat exchanger (PHX). Further, the propagation of melt and freeze front were experimentally determined in a 3D printed shell and tube heat exchanger. A horizontal configuration was used for both HX in this study.

From the experiments, it could be observed that the average power during melting is consistently higher than the corresponding values during solidification for a given flow rate. This is consistent among all the heat exchangers tested in this study. The enhancement of power rating and the effectiveness for the melting process was thus correlated to the reduction in the overall effective resistance during heat transfer between the PCM and HTF (due to the onset of natural convection).

A higher effectiveness and power rating could be observed at identical flow rates for the chevron plate heat exchanger in comparison to that of the shell and tube heat exchanger due to the higher effective heat transfer area between the HTF and PCM (~0.09 m^2 vs ~0.05 m^2). This is in addition to the lower mass of PCM. Also, stacking the HTF in between alternating layers of PCM adds to the favorable performance of the plate heat exchanger. Additionally, the enhancement in the power was found to be more sensitive to the flow rate in comparison to that of the inlet temperature of the HTF.

In case of the 3D printed shell and tube heat exchanger, it can be seen that the melt front is influenced by the buildup of HTF at the inlet and the outlet manifold. Hence, the region of PCM in contact with the inlet and outlet manifold melts before the PCM in the central part of the heat exchanger. Even though, a radially outward melt pattern could be realized, the effect of natural convection leads to accumulation of melt at the top of the shell and hence the PCM at the top melts first while the PCM at the bottom melts last. At steady state (after compete melting), a significant thermal gradient (~ 3°C) could also be observed due to stratification.

The propagation of freeze front is fairly straightforward within the PCM region closest to the inlet, causing a radially outward propagation of freeze front as the solidification progresses. It could also be observed that at higher flow rates, the variation in the phase transition time for all the radial locations within the region of influence of the HTF tube array is minimal. Hence, one can expect the PCM trapped in the HTF tube array to solidify almost uniformly at higher flow rates followed by a radially outward progression of the freeze front.

4.2 Conclusion

The following are the conclusions derived from this study:

- The average power rating for both HX was consistently higher for melting process in comparison to that of the solidification process due to the dominance of natural convection during melting.
- The average power rating for both the melting and solidification process for the plate exchanger increases at higher flow rate and is more sensitive to the values of the inlet temperature of HTF. The average power was more sensitive to the flow rate than the inlet temperature of HTF.
- Effectiveness for the heat exchangers were found to be higher at lower flow rates due to the higher ΔT_{HTF}. This is because the heat exchanger effectiveness is directly proportional to the observed ΔT_{HTF} which in turn is higher at lower flow rates due to average residence time inside the heat exchanger.
- For the flow rates and inlet temperatures of HTF used in the experiments, Chevron Plate Heat Exchanger had a higher average melt power rating and effectiveness due to the higher heat transfer area to PCM mass.
- The propagation of melt and freeze fronts are not identical for the 3D printed shell and tube heat exchanger.
- For the melting process, PCM near the inlet and outlet manifolds complete phase transition first. There is a radially outward propagation of melt front observed during the experiments for shell and tube heat exchangers. However, since the effect of natural convection heat

transfer is expected during melting, it is highly likely that the propagation was influenced by the convection and accumulation of melted PCM at the top of the heat exchanger.

- During solidification, the propagation of the freeze front is very predictable with the freezing of PCM occurring first at the inlet of the heat exchanger followed by a radially outward propagation of the freeze front in the heat exchanger.
- At higher flow rates, it can be expected that the PCM embedded in the HTF tube array will freeze uniformly and independent of the radial location (for locations closer to the tubes). However, a significant delay in the phase change is observed at radial locations far from the array of HTF tubes.

4.3 Recommendations

Based on the observations from the study, the following recommendations are provided to optimize the performance characteristics of the heat exchangers as well as on topics for future studies:

1. The maximum power rating of the 3D printed heat exchanger was determined to be lower than the commercially available plate heat exchanger. This is because the effective heat transfer area between the HTF and the PCM was significantly lower for the 3D printed shell and tube heat exchanger. To ensure a better performance of the 3D printed shell and tube heat exchangers, modifications such as addition of fins to the HTF tubes, usage of metal mesh matrices within the PCM containment and other techniques discussed in section 1.4.1 could be utilized. This would enhance the net heat transfer during the cycle by reducing the thermal resistance in the LHTESS and by increasing the thermal conductivity of the PCM. However, it should be noted that the 3D Printed heat exchanger has a higher TES capacity owing to the larger mass of PCM loaded into the HX.
2. The use of salt hydrates in the heat exchangers could enhance the energy storage capacity for the same phase transition temperature. Since one of the major drawbacks of using salt hydrates in commercially available heat exchanger is the effect of corrosion on metals, incorporation of salt hydrates into a 3D printed containment is both economical and advantageous.
3. Incorporation of machine learning algorithms to predict the melt propagation for LHTESS involving salt hydrates could improve the efficacy of the conventional cold fingering technique to alleviate sub cooling issues in salt hydrates.

4. The propagation of melt and freeze fronts could also be observed by using a transparent acrylic shell which offers similar thermal advantages as that of a 3D printed shell.
5. The prediction of melt and free front propagation could be performed using a suitable computation fluid dynamics (CFD) simulation.
6. Comparison of the performance of the shell and tube heat exchangers for horizontal and vertical orientation could be performed to ascertain the variation in the thermal performance characteristics of the heat exchanger and to observe the corresponding profiles for melt and freeze front propagation.

REFERENCES

A. Sharma, V. V. Tyagi, C. Chen, and D. Buddhi. 2009. "Review on Thermal Energy storage with Phase Change Materials and Applications." *Renewable and Sustainable Energy Reviews* 13 (2): 318-345.

A.Abhat. 1983. "Low Temperature latent heat temperature energy storage: heat storage materials." *Solar Energy* 30 (4): 313-332.

Abhat, A. 1981. *Development of a Modular Heat Exchnager with Intergrated Latent Heat Stroeg (in German).* Germany: German Ministry for Science and Technology.

Akgün, M., Aydın, O., & Kaygusuz, K. 2007. "Experimental study on melting/solidification characteristics of a paraffin as PCM. Energy Conversion and Management." 48(2): 669–678.

Akgün, M., Aydın, O., & Kaygusuz, K. 2008. "Thermal energy storage performance of paraffin in a novel tube-in-shell system." *Applied Thermal Engineering* 28(5): 405–413.

B. C. Shin, S. D. Kim and W.-H. Park. 1989. "Phase separation and supercooling of a latent heat-storage material." *Energy* 14: 921-930.

B. G. Ramirez, C. Glorieux, E. S. M. Martinez and J. F. Cuautle. 2014. "Tuning of Thermal Properties of Sodium Acetate Trihydrate by blending with polymer and Silver nanopartilces." *Applied Thermal Engineering* 62 (2): 838-844.

B. Zalba, J. M. Marın, L. F. Cabeza, and H. Mehling. 2003. "Review on thermal energy storage with phase change: materials, heat transfer analysis and applications." *Applied Thermal Engineering* 23 (3): 251-283.

Banerjee, M. K. Rathod and J. 2013. "Thermal stability of phase change materials used in latent heat energy storage systems: a review." *Renewable and Sustainable Energy Reviews* 18: 246-258.

Danilin, V. N. 1981. USSR Patent 842094.

Dincer, M. Rosen and Ibrahim. 2002. *Thermal Energy Storage, Systems, and Applications.* Chichester (England): Johm Wiley & Sons.

E. Gunther, H. Mehling and M. Werner. 2007. "Melting and Nucleation Temperatures of Three Salt Hydrates phase change materials under static pressures up to 800 MPA." *Journal of Physics: Applied Physics* 40: 4636-4641.

F.A.Kulacki. 2018. *Handbook of Thermal Science and Engineering.* Springer.

Gawron, J. Schroder and K. 1980. Heat Stroage Material Comprising Calcium Chloride-Hexahydrate and a Nucleating Agent. United States of America Patent 4189394. Feb 19.

Gong, Z, Mujumdar A. S. 1997. "Finite-element analysis of cyclic heat transfer in a shell and tube latent heat energy storage exchanger." *Applied Thermal Engineering* 17 (4): 583–91.

Goswami, T. Pirasaci and D. Y. 2016. "Influence of design on performance of a latent heat storage system for a direct steam generation power plant." *Applied Energy* 162: 644-652.

H. W. Ryu, S. W. Woo, B. C. Shin and S. D. Kim. 1992. "Prevention of Supercooling and stabilization of inorganic salt hydrates as latent heat storage materials." *Solar Energy Materials and Solar Cells* 27 (2): 161-172.

I.M. Rasta, I.N. Suamir. 2018. "The role of begetable oil in water based phase chnage materials for medium temperature refrigeration." *Journal of Energy Storage* 15: 368-378.

J. García-Alonso, F. Aguilar, and E. Montero. 2014. "Heat transfer with phase change in a shell and tube latent heat storage unit." *International Conference on Heat Transfer, Fluid Mechanics and Thermodynamics.*

J. Shon, H. Kim, and K. Lee. 2014. "Improved heat storage rate for an automobile coolant waste heat recovery system using phase-change material in a fin–tube heat exchanger." *Applied Energy* 113: 680-689.

Joybari, M. M., & Haghighat, F. 2016. "Natural convection modelling of melting in phase change materials: Development of a novel zonal effectiveness-NTU." *9th International Conference on Indoor Air Quality Ventilation and Energy Conservation in Buildings.*

Joybari, M. M., Haghighat, F., & Seddegh, S. 2017. "Numerical investigation of a triplex tube heat exchanger with phase change material: Simultaneous charging and discharging. Energy and Buildings." 139: 426–438.

K. Birkinshaw, M. Marwan and R. L. Therkelsen. 2002. *Comparsion of Alternate Cooling Technologies for California Power Plants Economic, Environmental and Other Tradeoffs.* California Energy Commission.

Kai, H. Kimura and J. 1984. "Phase Change Stability of CaCl2.6H2O." *Solar Energy* 1: 49-55.

Kumar, Navin. 2018. "Experimental Investigation of Latent Heat Energy Storage System (LHTESS) for enhancing performance of dry-cooling powerplant."

L. F. Cabeza, G. Svensson, S. Hiebler and H. Mehling. 2003. "Thermal performance of sodium acetate trihydrate thickened with different materials as phase change energy storage material." *Applied Thermal Engineering* 23: 1697-1704.

L. Ying, B.-Y. Chen, C.-c. Sun and X.-H. Zhang. 2008. "Study on Influence Factors of Thermal Hysteresis in Parafin Actuator." *IEEE Computer Society.*

Lane, G. A. 1992. "Phase Change Materials for Energy Stroage Nucleation to Prevent Supercooling." *Solar Energy Materials and Solar Cells* 27: 135-160.

Lane, G. 1983. *Background and Scientific Principles in Solar Heat Storage: Latent Heat Material vol.I.* Florida: CRC Press.

Longeon, M., Soupart, A., Fourmigué, J.-F., Bruch, A., & Marty, P. 2013. "Experimental and numerical study of annular PCM storage in the presence of natural convection." *Applied Energy* 112: 175–184.

M. A. Shamseldin, F. A. Al_Sulaiman, N. I. Ibrahim and A. Z. Sahin. 2017. "A review on current status and challenges of inorganic phase change materials for thermal energy storage systems." *Renewable and Sustainable Energy Reviews* 70: 1072-1089.

M. E. H. Amagour, A. Rachek, M. Bennajah, and M. E. Touhami. 2018. "Experimental investigation and comparative performance analysis of a compact finned-tube heat exchanger uniformly filled with a phase change material for thermal energy storage." *Energy Conversion and Management* 165: 137-151.

M. Hosseini, M. Rahimi, and R. Bahrampoury. 2014. "Experimental and computational evolution of a shell and tube heat exchanger as a PCM thermal storage system." *International Communications in Heat and Mass Transfer* 50: 128-136.

M. Hosseini, M. Rahimi, and R. Bahrampoury. 2015. "Thermal analysis of PCM containing heat exchanger enhanced with normal annular fins p." *Mechanical Sciences* 6 (2): 221.

M. M. Farid, A. M. Khudhair, S. A. K. Razack and S. Al-Hallaj. 2004. "A Review on Phase Change Energy Stroage: Materials and Applications." *Energy Conversion and Management* 45 (9-10): 1597-1615.

M. Medrano, M. Yilmaz, M. Nogués, I. Martorell, J. Roca, and L. F. Cabeza. 2009. "Experimental evaluation of commercial heat exchangers for use as PCM thermal storage systems." *Applied Energy* 86 (10): 2047-2055.

M.K. Rathod, J.Banerjee. 2014. *Thermal Performance of a Phase Change Material-Based Latent Heat Thermal Storage Unit.* Vol. 43 . Heat Transfer—Asian Research.

Murray, R. E., & Groulx, D. 2014. "Experimental study of the phase change and energy characteristics inside a cylindrical latent heat energy storage system: Part 1 consecutive charging and discharging." *Renewable Energy* 62: 571–581.

N. I. Ibrahim, F. A. Al-Sulaiman, S. Rahman, B. S. Yilbas, and A. Z. Sahin. 2017. "Heat transfer enhancement of phase change materials for thermal energy storage applications: A critical review ." *Renewable and Sustainable Energy Reviews* 74: 26-50.

N. Kousha, M. Hosseini, M. Aligoodarz, R. Pakrouh, and R. Bahrampoury. 2017. "Effect of inclination angle on the performance of a shell and tube heat storage unit–An experimental study." *Applied Thermal Engineering* 112: 1497-1509.

O'Malley, P. J. Shamberger and M. J. 2015. "Heterogeneous nucleation of thermal stroage material LiNO3.3H2O from stable lattice-matched nucleation catalysts." *ACta Materialia* 265-274.

Rossow, G. A. Lane and H. E. 1979. Hydrated Mg(NO3)2 Reversible Phase Change Compositions. USA Patent 4271029.

S. Seddegh, M. M. Joybari, X. Wang, and F. Haghighat. 2017. "Experimental and numerical characterization of natural convection in a vertical shell-and-tube latent thermal energy storage system." *Sustainable Cities and Society* 35: 13-24.

S.Fleicher, A. 2015. "Thermal Energy Storage Using Phase Change Materials Fundamentals and Applications." *New York: SpringerBriefs in Thermal Engineering and Applied Science.*

Sarviya, A. Agarwal and R. 2016. "An experimental investigation of shell and tube latent heat storage for solar dryer using paraffin wax as heat storage material." *Engineering Science and Technology, an International Journal* 19: 619-631.

Schroder, J. 1980. *Systems for Thermal Energy Stroage in temperature range from -25°C to 150°C.* Brussels: Seminar New Ways to Save Energy.

Simmons, E. Williams and J. 2013. "Water in the Energy Industry." *BP*.

Trp, A. 2005. "An experimental and numerical investigation of heat transfer during technical grade paraffin melting and solidification in a shell-and-tube latent thermal energy storage unit." *Solar Energy* 79(6): 648–660.

Y. Tao, Y. Liu, and Y.-L. He. 2017. "Effects of PCM arrangement and natural convection on charging and discharging performance of shell-and-tube LHS unit." *International Journal of Heat and Mass Transfer* 115: 99-107.

Yazici, M. Avci and M. Y. 2013. "Experimental study of thermal energy storage characteristics of a paraffin in a horizontal tube-in-shell storage unit." *Energy conversion and management* 73: 271-277.

APPENDIX A

Shell and Tube Heat Exchanger (single point temperature measurement)

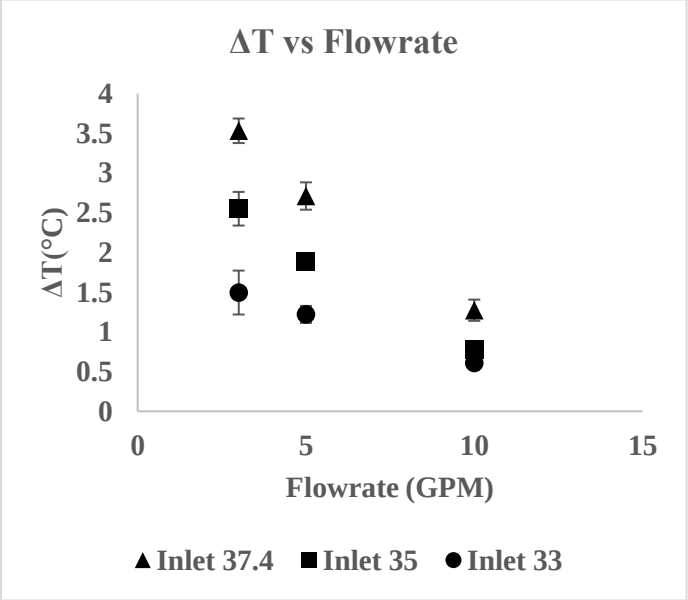

A- 1 Variation of ΔT with flow rate of HTF during melting

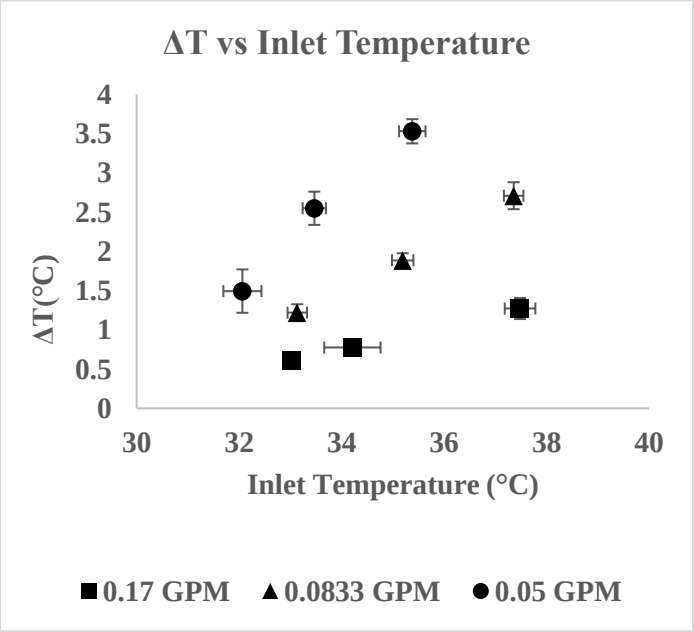

A- 2 Variation of ΔT with inlet temperature of HTF during melting

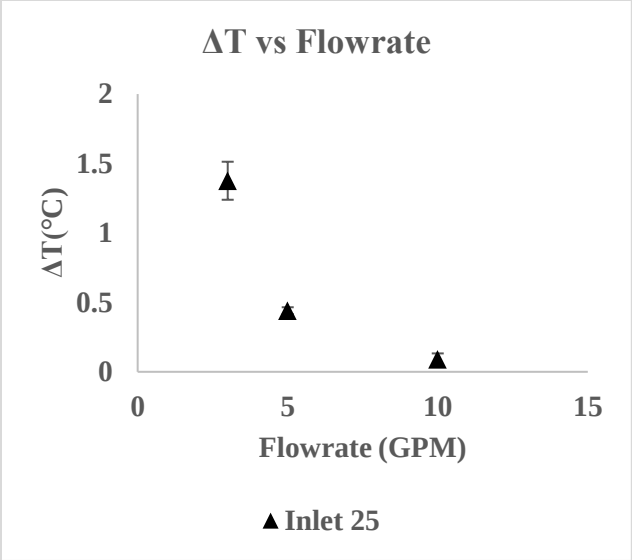

A- 3 Variation of ΔT with flowrate for solidification

A- 4 Summary of experimental results for 3D printed Shell and Tube Heat Exchanger (Single point temperature measurement)

Flow Rate (GPH)	Inlet Temperature (°C)	Process	Average Power (W)	Average ΔT (°C)	Average Effectiveness
3	33	Melting	20.19	1.49	0.79
3	35	Melting	33.32	2.55	0.75
3	37	Melting	44.84	3.53	0.75
5	33	Melting	24.11	1.22	0.39
5	35	Melting	39.35	1.89	0.43
5	37	Melting	59.45	2.71	0.46
10	33	Melting	26.34	0.61	0.20
10	35	Melting	52.44	1.27	0.23
10	37	Melting	52.44	1.27	0.23
3	25	Solidification	18.03	1.38	0.96
5	25	Solidification	9.99	0.44	0.39
10	25	Solidification	3.93	0.09	0.05

Chevron Plate Heat Exchanger

A- 5 Summary of experimental results for Chevron Plate Heat Exchanger

Flow Rate (GPH)	Inlet Temperature (°C)	Process	Average Power (W)	Average Effectiveness
5	38	Melting	36.32	0.61
5	34	Melting	28.62	0.69
5	32	Melting	24.23	0.98
8	38	Melting	56.55	0.63
8	34	Melting	52.95	0.67
8	32	Melting	28.50	0.63
10	38	Melting	91.92	0.64
10	34	Melting	70.71	0.74
10	32	Melting	52.78	0.73
5	20	Solidification	33.34	0.73
5	24	Solidification	20.36	0.92
5	26	Solidification	12.53	0.71
8	20	Solidification	52.75	0.73
8	24	Solidification	24.68	0.70
8	26	Solidification	19.58	0.67
10	20	Solidification	71.87	0.64
10	24	Solidification	39.73	0.74
10	20	Solidification	32.22	0.73

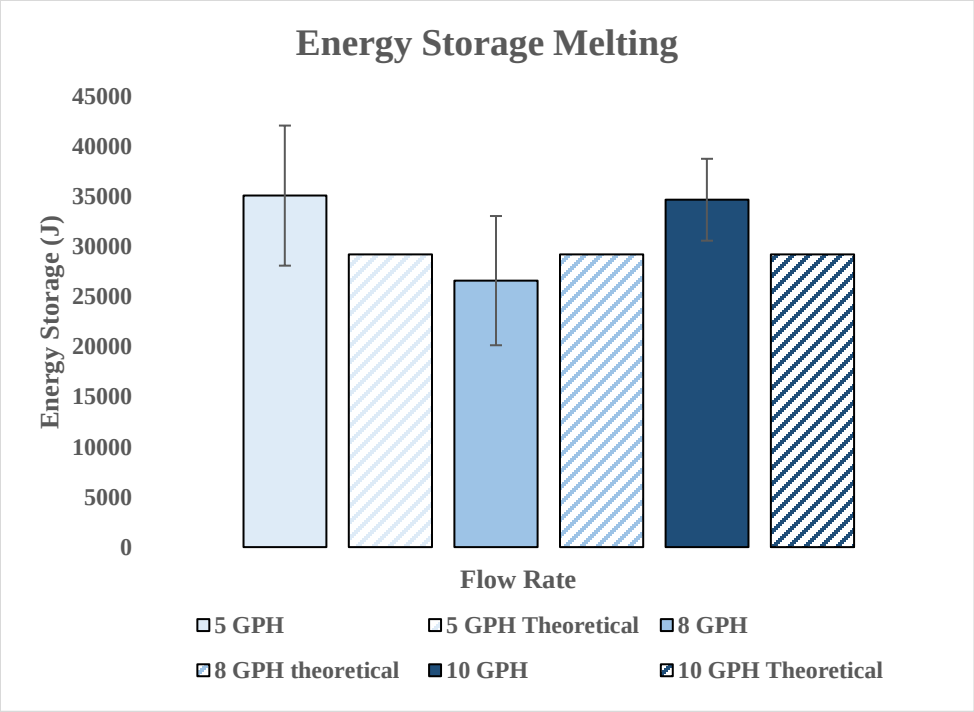

A- 6 Actual and theoretical energy storage for inlet temperature of 32°C (Melting)

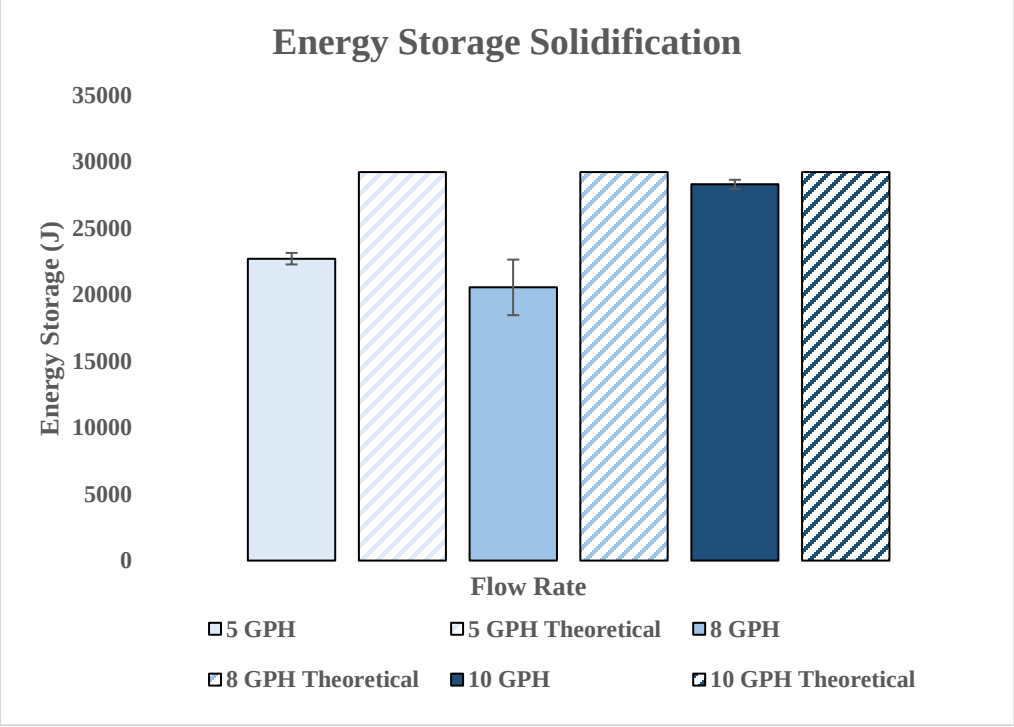

A- 7 Actual and theoretical energy storage for inlet temperature of 26°C (Solidification)

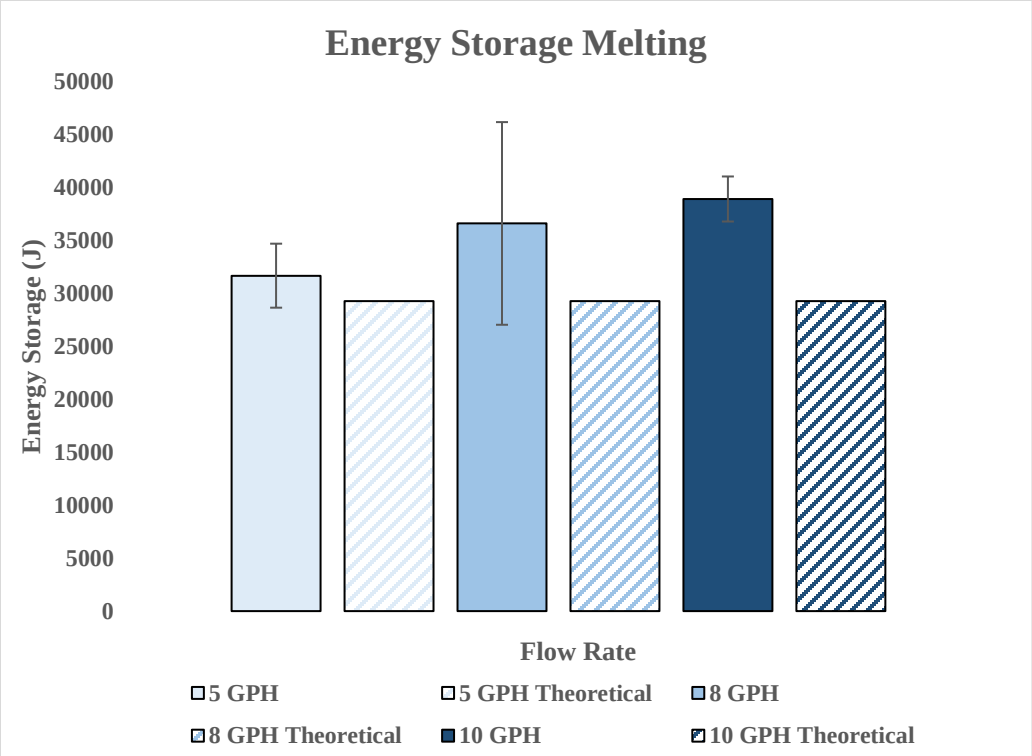

A- 8 Actual and theoretical energy storage for inlet temperature of 34°C (Melting)

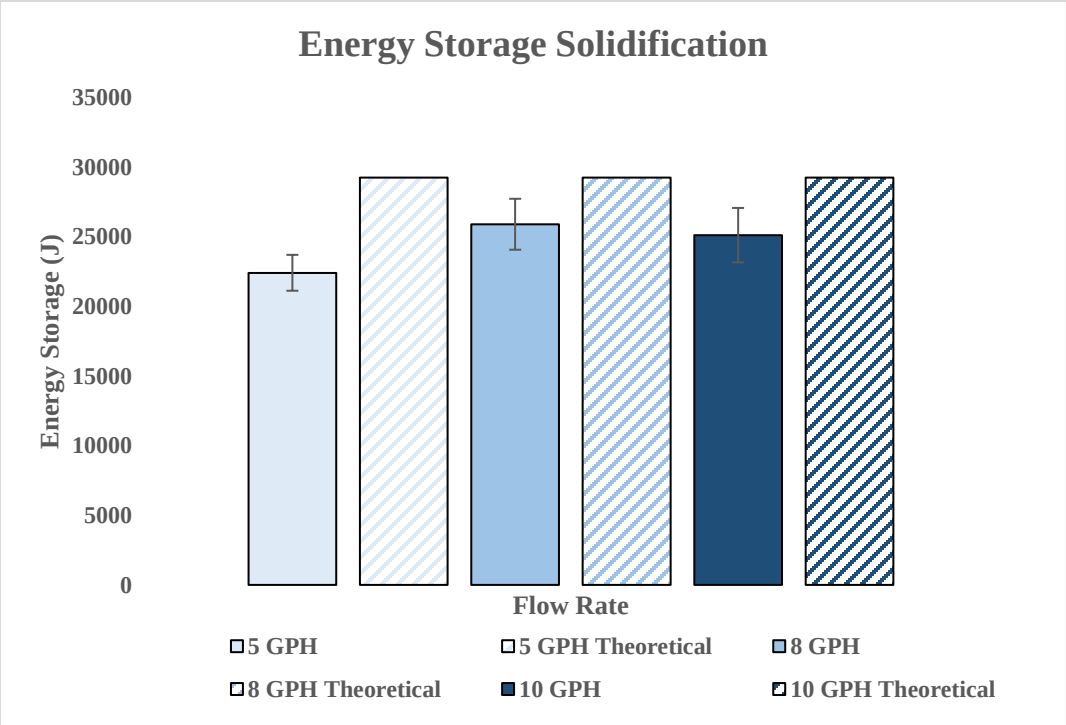

A- 9 Actual and theoretical energy storage for inlet temperature of 24°C (Solidification)

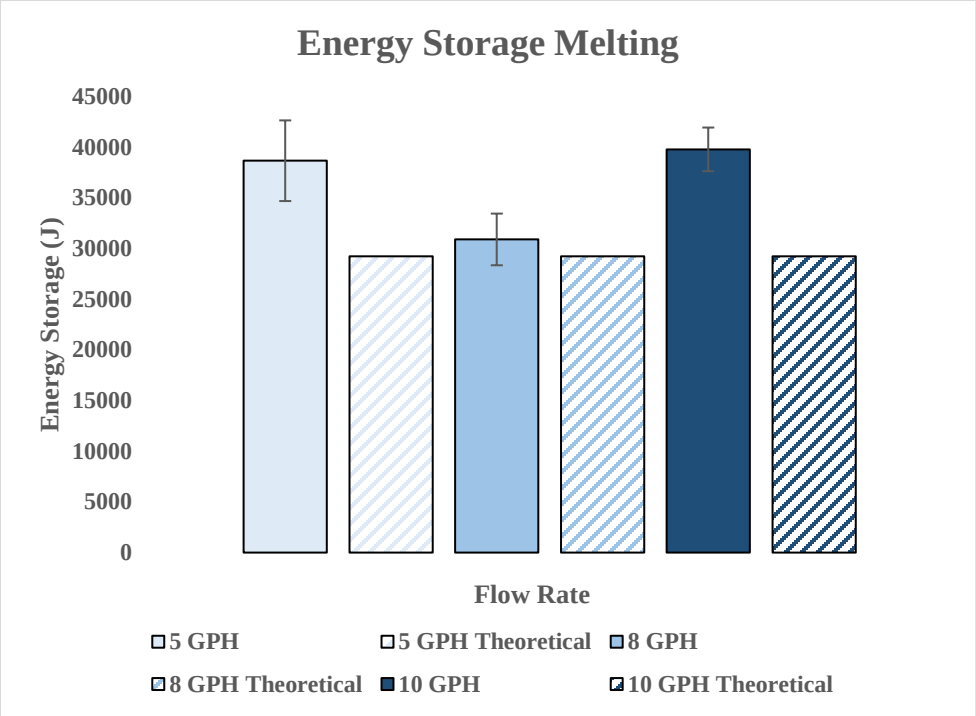

A- 10 Actual and theoretical energy storage for inlet temperature of 38°C (Melting)

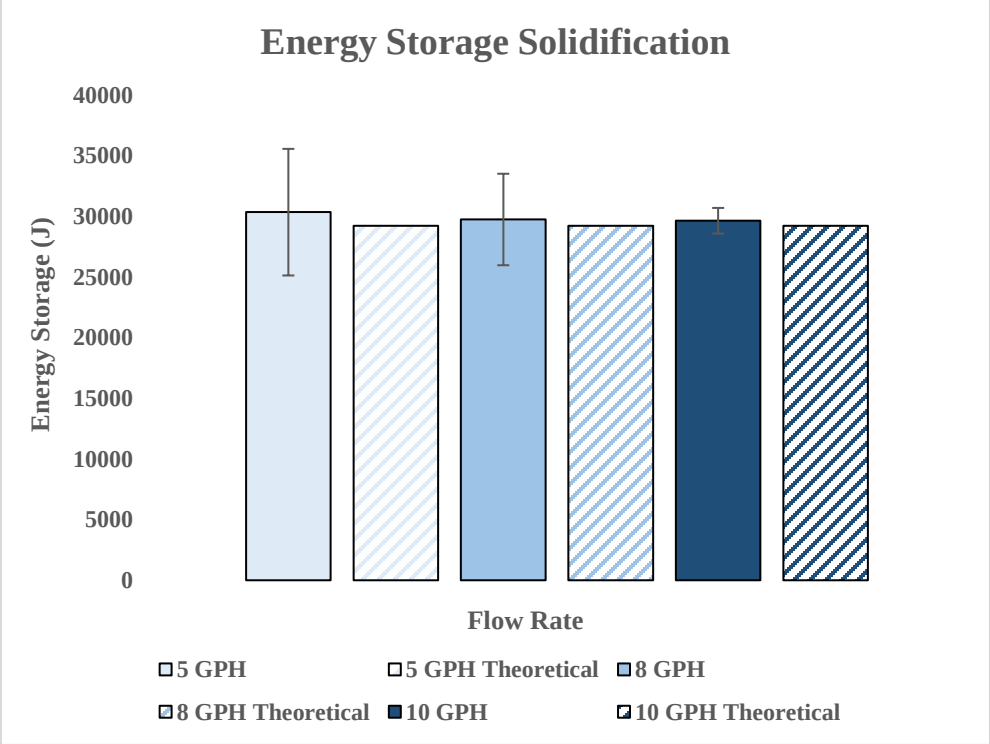

A- 11 Actual and theoretical energy storage for inlet temperature of 20°C (Solidification)

Shell and Tube Heat Exchanger (12 point axial and radial temperature mapping)

A- 12 Position of thermocouples in the 3D printed shell and tube heat exchanger

Thermocouple Locations from Horizontal	Inlet TCs	Mid TCs	Outlet TCs	Thermocouple Vertical Position
45°	TC 1	TC 5	TC 9	Mid-Level-1 (Closer to Top)
135°	TC 2	TC 6	TC 10	Top
225°	TC 3	TC 7	TC 11	Mid-Level-2 (Closer to Bottom)
315°	TC 4	TC 8	TC 12	Bottom

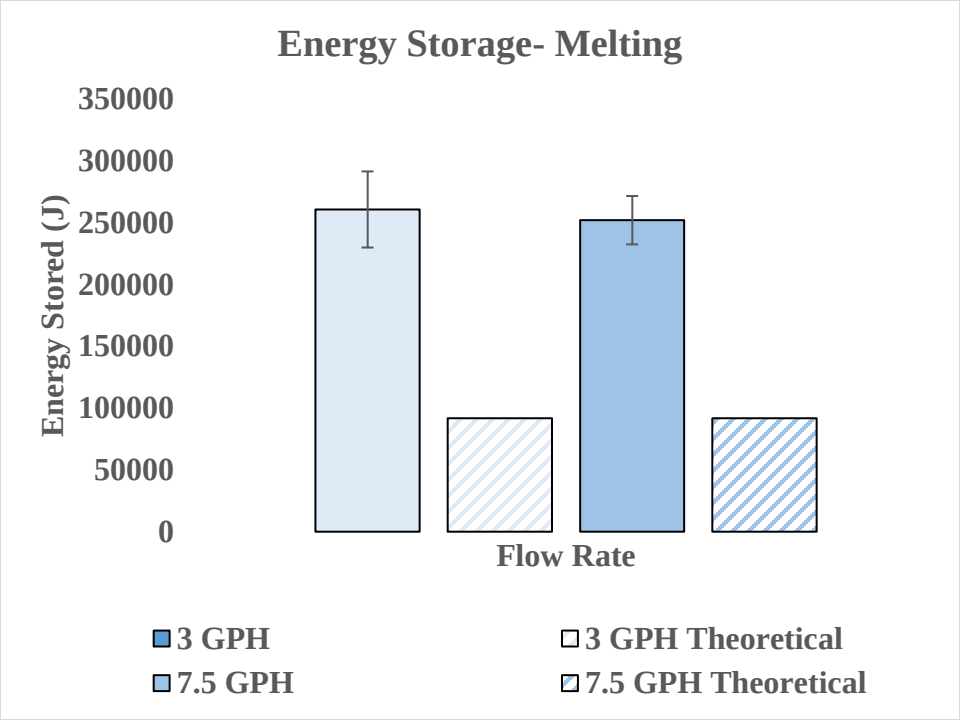

A- 13 Actual vs theoretical energy storage during melting for inlet temperature 38°C

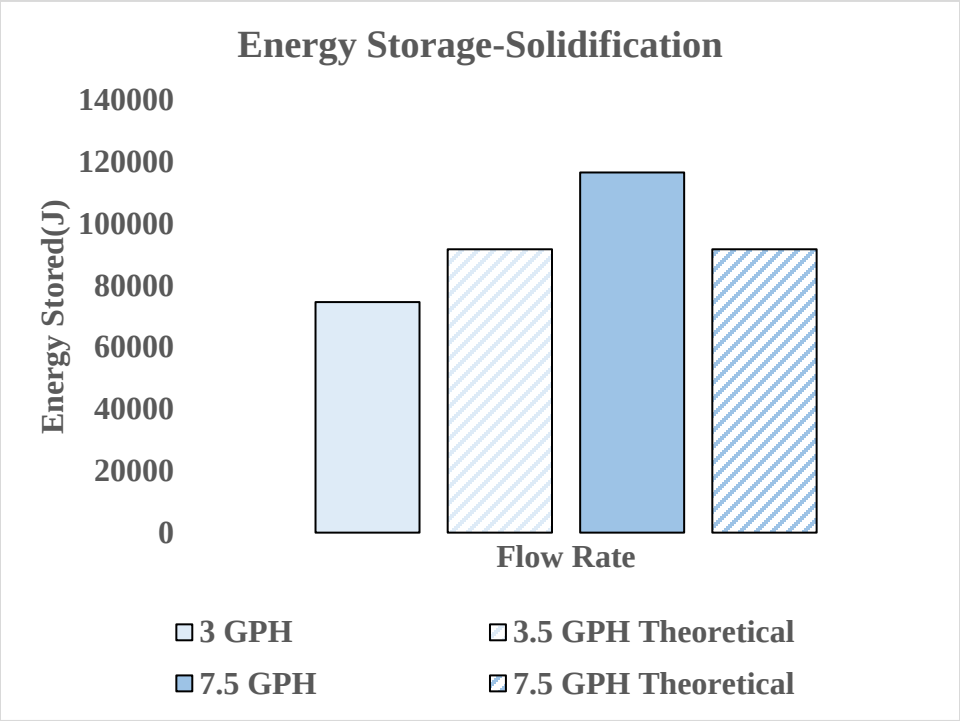

A- 14Actual vs theoretical energy storage during solidification for inlet temperature 20°C

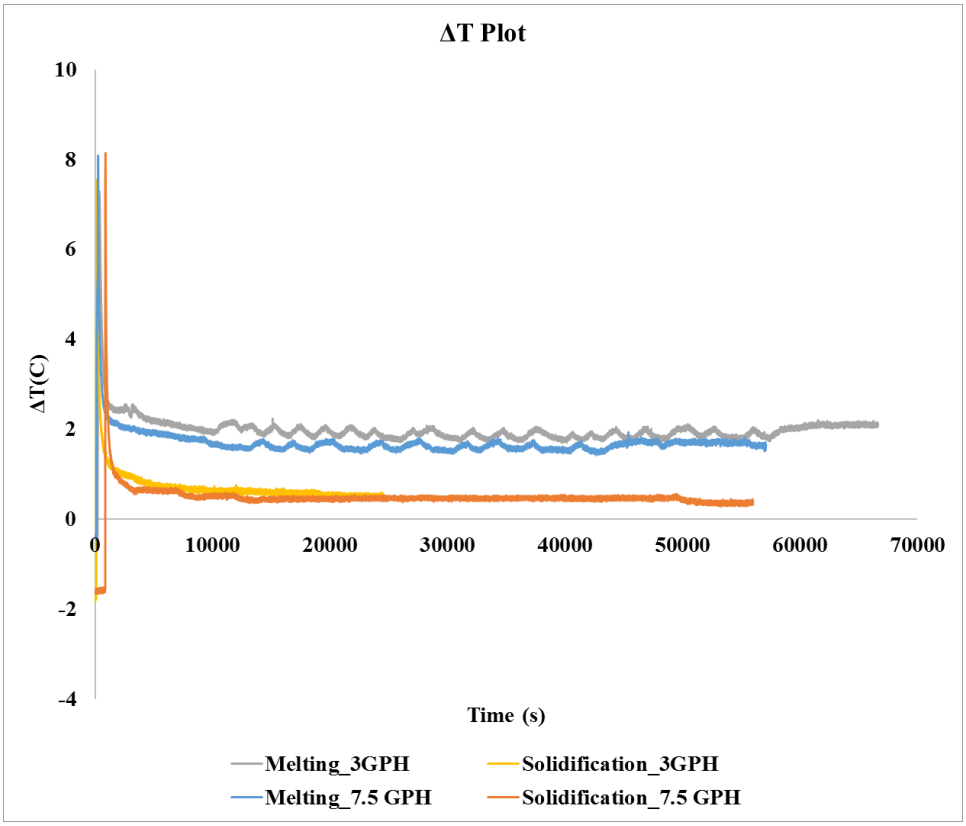

A- 15 Instantaneous ΔT for melting and solidification

APPENDIX B

Challenges

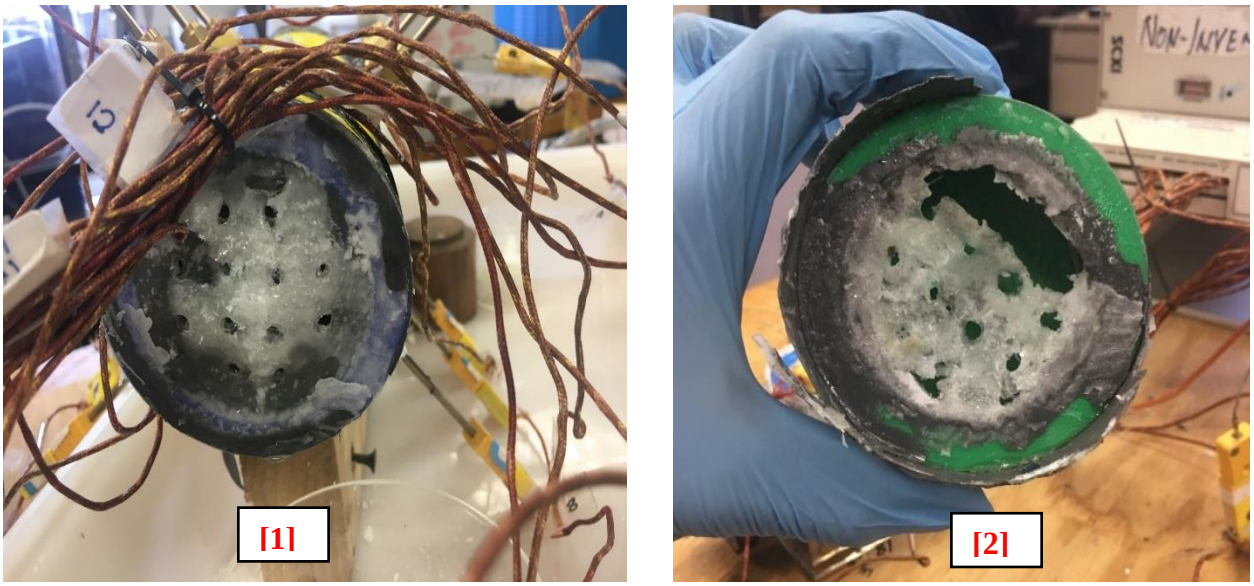

A- 16 [1] Deposition of PCM on the plate separating the inlet manifold and PCM Shell [2] PCM deposition in the inlet manifold

The experiments conducted on the 3D printed Shell and Tube Heat Exchanger (12 point temperature measurement) was impacted by the mixing of PCM from the shell with the water in the inlet and outlet manifold. The porosity of the 3D printed plates separating the PCM shell from the manifold led to the unintended mixing of the media. This impacted the repeatability of the experiments. Seepage of PCM through the shell was also observed during melting.

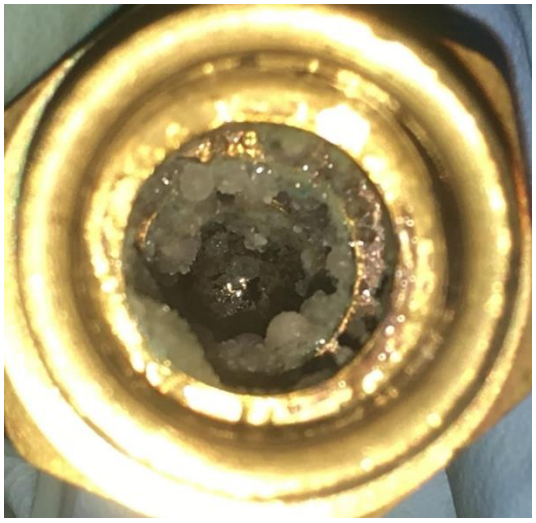

A- 17 Deposition of solid PCM on the walls of a connector used in the experiment

Additionally, the contamination of water with PCM during melting, caused deposition of solid PCM during solidification on the walls of the tubing and other connectors thereby restricting the flow passage.